

REPORT DOCUMENTATION PAGE

AFRL-SR-AR-TR-04-

0252

Public reporting burden for this collection of information is estimated to average 1 hour per response, including the time for reviewing instructions, searching existing data sources, gathering the required data, reviewing the collection of information, sending comments regarding this burden estimate or any other aspect of this collection of information, including suggestions for reducing the burden, to Washington Headquarters Services, Directorate for Information Operations and Reports (0704-01 4302). Respondents should be aware that notwithstanding any other provision of law, no person shall be subject to any penalty for failing to comply with a collection of information if it does not display a currently valid OMB control number. PLEASE DO NOT RETURN YOUR FORM TO THE ABOVE ADDRESS.

1. REPORT DATE (DD-MM-YYYY) 31-03-2004		2. REPORT TYPE Final Technical		3. DATES COVERED (From - To) 1-12-2000 - 31-12-2003	
4. TITLE AND SUBTITLE (U)Mixing, Chemical Reactions, and Combustion in High-Speed Turbulent Flows				5a. CONTRACT NUMBER	
				5b. GRANT NUMBER F49620-01-1-0006	
				5c. PROGRAM ELEMENT NUMBER 61102F	
6. AUTHOR(S) Paul E. Dimotakis				5d. PROJECT NUMBER 2308	
				5e. TASK NUMBER BV	
				5f. WORK UNIT NUMBER	
7. PERFORMING ORGANIZATION NAME(S) AND ADDRESS(ES) Aeronautics, Mail Code 301-46 California Institute of Technology 1200 E. California Boulevard Pasadena, CA 91125				8. PERFORMING ORGANIZATION REPORT NUMBER	
9. SPONSORING / MONITORING AGENCY NAME(S) AND ADDRESS(ES) AFOSR/NA 4015 Wilson Blvd., Room 713 Arlington VA 22203-1954				10. SPONSOR/MONITOR'S ACRONYM(S)	
				11. SPONSOR/MONITOR'S REPORT NUMBER(S)	
12. DISTRIBUTION / AVAILABILITY STATEMENT Approved for public release; distribution is unlimited					
13. SUPPLEMENTARY NOTES					
14. ABSTRACT Research conducted under the sponsorship of this grant focused on fundamental investigations of mixing, chemical-reaction and combustion processes; in turbulent, subsonic, and supersonic flows. Research on hydrocarbon-combustion was on methane and ethane flames. Flame extinction strain-rate measurements, flame speed, and detailed experiment-simulation comparisons indicate difficulties in modeling of fuel-rich flames. Direct Numerical Simulations (DNS) of axisymmetric unsteady flows in both cold and hot impinging jets were also performed. The research included work on high-speed internal flows of interest to scramjet mixing and combustion, aimed at flow-control and flameholding issues. DNS and Large Eddy Simulations (LES) of Rayleigh-Taylor instability flows studied Reynolds number effects on mixing in this important flow. Advances in high-performance digital-imaging systems were transferred to the laboratory environment enabling measurements unachievable by other means.					
15. SUBJECT TERMS Combustion, mixing, subsonic, supersonic, turbulence, hydrocarbon flames, Rayleigh-Taylor instability, high-speed digital imaging.					
16. SECURITY CLASSIFICATION OF:			17. LIMITATION OF ABSTRACT	18. NUMBER OF PAGES	19a. NAME OF RESPONSIBLE PERSON Dr. Julian Tishkoff
a. REPORT Unclassified	b. ABSTRACT Unclassified	c. THIS PAGE Unclassified			19b. TELEPHONE NUMBER (include area code) (703) 696-8478
			UL	37	

20040520 056

GRADUATE AERONAUTICAL LABORATORIES
CALIFORNIA INSTITUTE of TECHNOLOGY
Pasadena, California 91125

Mixing, chemical reactions, and combustion in high-speed
turbulent flows

Paul E. Dimotakis, Principal Investigator

Air Force Office of Scientific Research
Grant No. F49620-01-1-0006

Final Scientific Report
1 December 2000 through 31 December 2003

DISTRIBUTION STATEMENT A
Approved for Public Release
Distribution Unlimited

31 March 2004

Summary

This is the final scientific report on research and work undertaken under the sponsorship of AFOSR Grant F49620-01-1-0006, on "Mixing, chemical reactions, and combustion in high-speed turbulent flows". The effort undertaken spans fundamental research areas in turbulent mixing, with and without chemical reactions and combustion, involving liquid- and gas-phase fluids, in both uniform-density and inhomogeneous flows, ranging from incompressible to compressible and supersonic flows. The work is experimental, augmented by an accompanying instrumentation and diagnostics effort, as well as computational and theoretical. Many crucial components of the research rely on a tight integration of experimental and numerical-simulation work.

Research summarized in the report below and in publications cited covers work on hydrocarbon stagnation flames and their extinction characteristics, mixing and combustion in complex compressible flows of generic interest to high-speed air-breathing hypersonic propulsion, and Rayleigh-Taylor Instability (RTI) flows, as well as work on digital imaging and high-speed data acquisition developments. The latter have played a major, if not crucial, role in all of the experimental projects documented here.

1 Hydrocarbon flames and combustion

1.1 Experiments

We report on a combined experimental and simulation effort studying strained premixed flames performed as part of this program. These flames are stabilized in a stagnation-flow configuration, similar to that used by Law et al. (1981). This geometry permits the establishment of premixed flames at a variety of imposed strain-rates and mixture compositions. In addition, stagnation flows can be simulated approximating the flow using a one-dimensional hydrodynamic model (Kee et al. 1988). Such simulations allow complex chemistry and species transport to be included without excessive computational cost. While such hydrodynamic models have been used in both theoretical (*e.g.* Libby 1998) and numerical (*e.g.* Egolfopoulos 1994) studies of premixed flames, few comparisons with experimental data are available. Experimental velocity and major species profiles are compared to numerical simulations in the work of Law and coworkers (Law et al. 1994; Sung et al. 1994, 1996a,b). In that work, the inlet velocity boundary conditions are adjusted to visually align the temperature and species profiles. While agreement is seen in the predicted profiles, partially validating the thermochemistry portion of the models, these studies do not test or validate the hydrodynamic aspects of the simplified one-dimensional model.

To assess the performance of the one-dimensional hydrodynamic model, a study of the cold impinging jet flow was first performed. Velocity profiles are measured using Particle Streak Velocimetry (PSV, Dimotakis et al. 1981). The pressure drop across the nozzle contraction is also measured and proves to be an important parameter in this flow. While this flow appears simple and regarded as well-documented, some new and important elements resulted from this study. It was found that the axial velocity profile along the jet centerline is essentially independent of the nozzle-stagnation plate separation distance, when scaled by the Bernoulli velocity (expressed below for an axisymmetric nozzle),

$$U_B \equiv \sqrt{\frac{2\Delta p}{\rho[1 - (r_2/r_1)^4]}} \quad (1)$$

where Δp is the pressure drop across the nozzle, ρ is the gas density, and r_2 and r_1 are the radii of the nozzle exit and inlet, respectively. Figure 1(a) depicts the axial velocity profile for a $Re = 700$

impinging jet, for three nozzle-plate separation distance. The collapsed velocity profiles are well approximated by a similarity expression in terms of an error function (Kostiuk et al. 1993),

$$\frac{u(x)}{U_B} = \text{erf} [\alpha (x - \delta) / d] \quad (2)$$

where $u(x)$ is the axial velocity, U_B is the Bernoulli velocity, α is a strain-rate parameter, x is the wall-normal distance, δ is a viscous boundary layer offset, and d is the nozzle diameter. Extensions to the work of Kostiuk et al. (1993) by our group have shown that only a few of these parameters are independent and that the velocity asymptotes to the Bernoulli velocity far from the plate. An example of this single-parameter fit is given in Fig. 1(b).

The velocity profiles given in Fig. 1(a) indicate that a free-jet region of the flow is established for nozzle-plate separation distances greater than $L/d \simeq 1$. The simplified one-dimensional hydrodynamic model cannot capture the hydrodynamics of such a flow and thus cannot simulate large L/d experiments (see Fig. 2(a)). However, good agreement is obtained if the boundary condition to the one-dimensional model is specified from the measured velocity profile in the stagnation region of the flow, as illustrated in Fig. 2(b).

To further validate the new PSV methodology developed as part of this study in a flame environment, laminar flame speeds were measured using the extrapolation method (Wu and Law 1984). Local measurements of the imposed strain-rate and the resulting reference flame speed are made using PSV. These reference flame speeds are extrapolated to zero strain-rate to give an estimate of the laminar flame speed (*cf.* Fig. 3(a)). Previous studies indicated that the extrapolation method overpredicts flame speeds because of nonlinearity in the response of the reference flame speed to stretch (Tien and Matalon 1991; Vagelopoulos et al. 1994). The measurements reported here were performed to validate the methodology against previous measurements. Figure 3(a) shows the data used in the extrapolation for a $\Phi = 0.71$ flame. Figure 3(b) plots the extrapolated data and

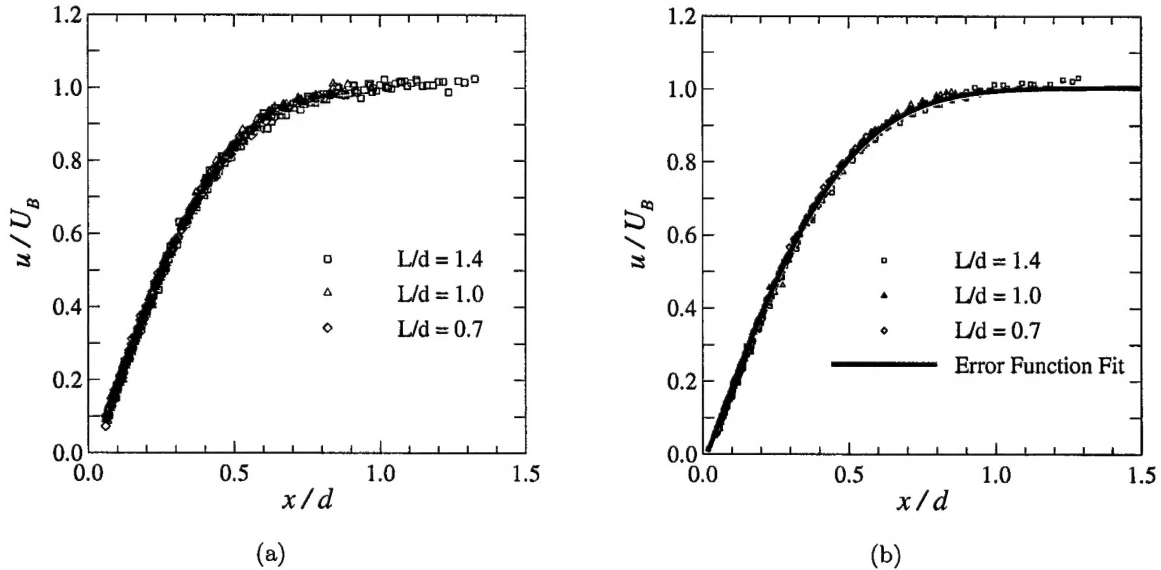


Figure 1: (a) Centerline axial velocity profile experimental results normalized by Bernoulli velocity, $Re = 700$. (b) Comparison of error-function fit to experimental data, $Re = 1400$.

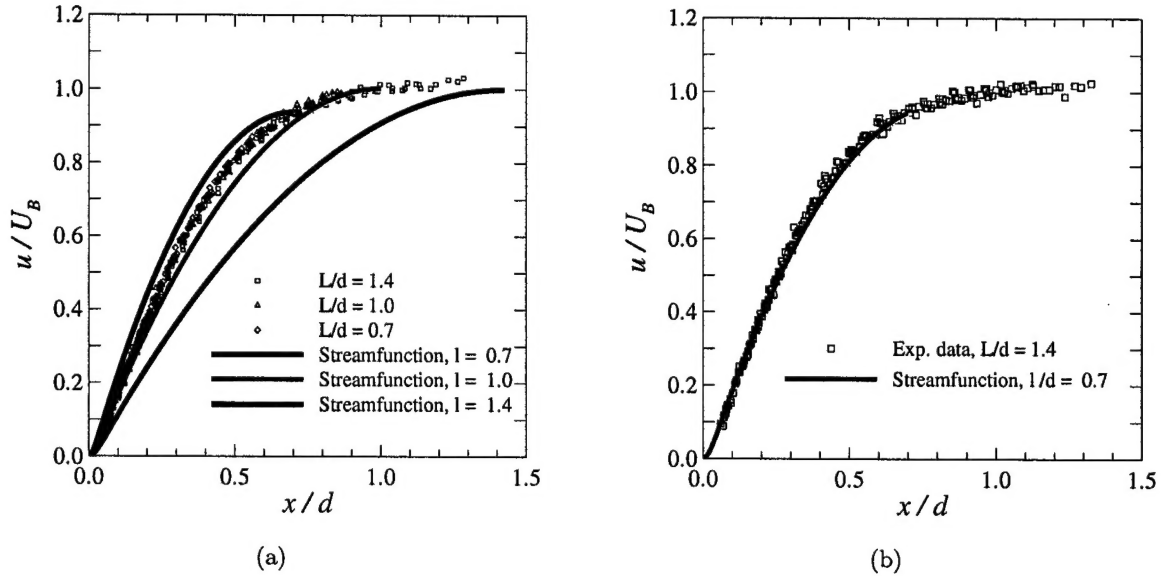


Figure 2: (a) Comparison of streamfunction simulation with plug-flow boundary conditions to experimental results at $Re = 1400$, varying l . (b) Comparison of streamfunction simulation to experimental data with velocity boundary conditions calculated from error-function fit to the data, $Re = 700$ and $l/d = 0.7$.

comparisons to previous data, and predictions by GRI-3.0 (Yamaoka and Tsuji 1984; Vagelopoulos et al. 1994; Smith et al. 2003).

Typically, the validation and development of chemical kinetic models have relied upon comparisons to global flame parameters, such as laminar flame speeds and extinction strain-rates. There is a large body of experimental data on laminar flame speeds for the low C-number fuels of interest in these studies (see Bosschaart and de Goey 2004). Extinction data are available only for select fuels and conditions (*e.g.* Yamaoka and Tsuji 1988; Konnov et al. 1996). Global flame properties at strain-rate extremes, *i.e.*, at zero strain rate (laminar flame speeds) and at the maximum achievable strain rates (extinction), have been employed as tests kinetic-transport models. Work begun as part of this program seeks to probe kinetic-transport models over the entire strain-rate regime, starting with ignition, low-to-high strain rates, up to extinction. To achieve this goal, a diagnostic suite was developed to make detailed velocity and CH-radical profile measurements in strained premixed flames stagnating against a fixed-temperature wall. Velocity measurements rely on PSV, as discussed above, that can be implemented with low-particle mass loading and still achieve high accuracy. Low particle loading minimizes disturbances to the flame, while, at the same time, reducing Mie-scattering noise in concurrent laser induced-fluorescence measurements.

CH profiles are measured using Planar Laser Induced Fluorescence (PLIF). CH was chosen as it is a short-lived radical that provides an accurate spatial marker of the reaction zone location. The PSV and CH PLIF diagnostics are complemented by concurrent measurements of the stagnation plate temperature, fuel, air and nitrogen diluent mass-flow rates, and the static pressure drop across the nozzle contraction. These measurements allow the specification of the temperature and species (equivalence ratio) boundary conditions in the numerical simulations.

Measurements for a near-stoichiometric ($\Phi = 0.9$) methane-air flame, at $L/d = 0.8$, are given in

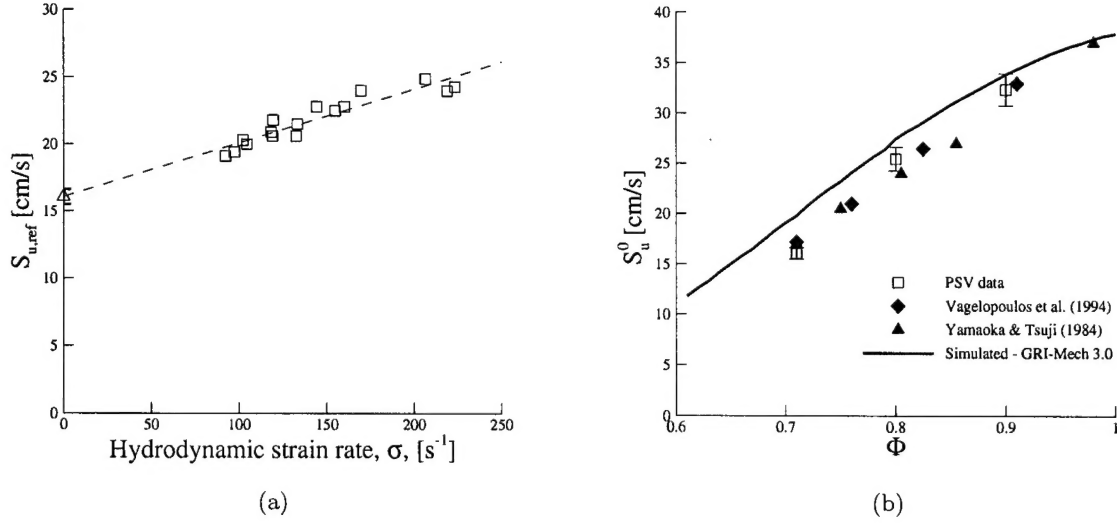


Figure 3: (a) Flame speeds, $S_{u,ref}$, vs. strain rate, σ , for a $\Phi = 0.71$, methane-air flame. Extrapolation to zero strain rate yields the laminar flame speed estimate, S_u^0 , and error bar. (b) Estimated laminar flame speeds of methane-air flames (squares). Data by Yamaoka and Tsuji (1984) (triangles) and Vagelopoulos et al. (1994) (diamonds). Numerical simulations use GRI-Mech 3.0 (line).

Fig. 4(a). These data are simulated numerically with the Cantera software package, developed by Goodwin (2003), and rely on the one-dimensional streamfunction formulation discussed above, and full chemistry (GRI-3.0) and species transport. Inlet velocity boundary conditions are specified from a fit to the cold-flow experimental data upstream of the flame. Good agreement is seen between experiments and simulations at this equivalence ratio.

To quantitatively compare simulation predictions with experiments, the difference is calculated between the measured and predicted peak CH concentration location, $x_{CH,PLIF}$ and $x_{CH,sim}$, scaled by the simulated CH-layer thickness, δ_{CH} . CH-layer thicknesses are calculated as the Full Width at Half Maximum (FWHM) of Gaussian fits to the simulated profiles. The difference between $x_{CH,PLIF}$ and $x_{CH,sim}$ is found to be less than $0.1 \delta_{CH}$, in this case.

To test the hydrodynamic model, the nozzle-plate separation distance was varied at this equivalence ratio. Predicted and experimental peak CH locations agree within $0.5 \delta_{CH}$ for $L/d = 0.6$ and 0.8 , and within $1.5 \delta_{CH}$ for $L/d = 1.0$ and 1.2 , at $\Phi = 0.9$. Experimental and predicted CH-peak locations exhibit reasonable agreement for near-stoichiometric mixtures ($\Phi = 0.9$), indicating good prediction of strained flame location for a variety of imposed hydrodynamic fields. The experiments also indicate that the simplified hydrodynamic model, as employed in these simulations, is adequate to capture the fluid mechanics of these flames. To our knowledge, this is the first study to simulate experimental flames with an accurate specification of the velocity boundary conditions, based on measured velocity profiles.

To investigate flame-temperature effects, a nitrogen-diluted $\Phi = 0.9$ flame is studied. Excess nitrogen is added to the premixture to reduce flame strength and temperature. Figure 4(b) shows good agreement between measured and predicted velocity and CH profiles, indicating that the simulations can accurately capture variations in flame heat release and attendant temperature-dependent transport effects. The difference between simulated and measured CH-peak locations is less than $0.1 \delta_{CH}$, in this case.

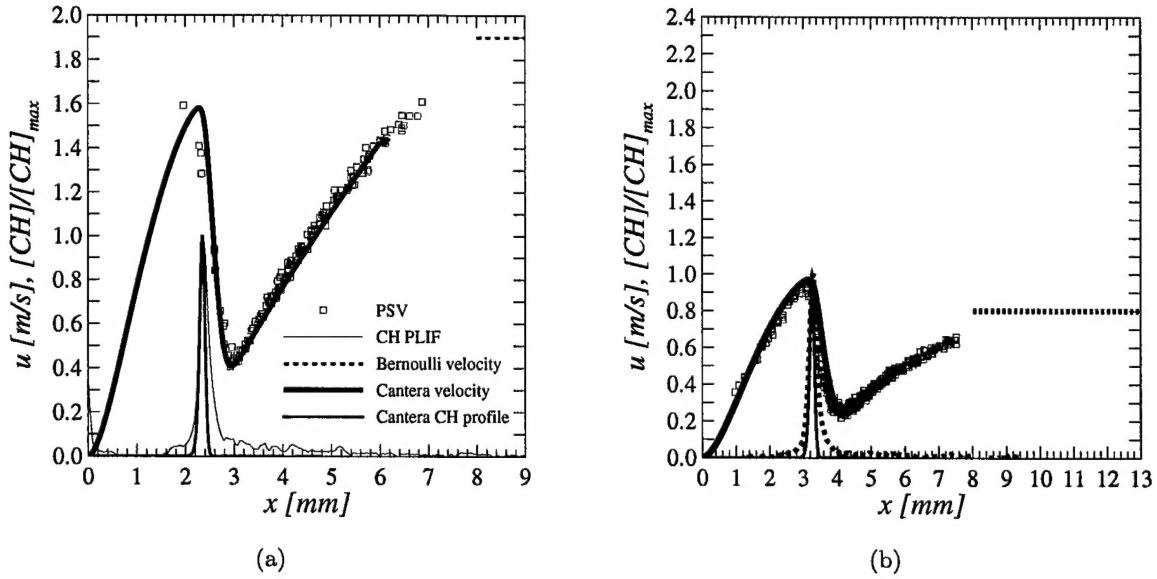


Figure 4: $\Phi = 0.9$, $L/d = 0.8$, methane-air flame profiles. Simulation boundary at $\ell = 6$ mm. (a) undiluted flame (b) nitrogen-diluted to 18% $O_2:(O_2+N_2)$.

Flame chemistry effects are probed by varying Φ . Representative results are given in Figs. 5(a) and 5(b). They compare experimental and predicted profiles for a lean and rich flame, respectively. For the lean flame ($\Phi = 0.63$), predicted CH-profile location is located closer to the stagnation plate than measured, consistent with an underprediction of strained-flame speed. Correspondingly, post-flame velocity is lower than measured. For the rich flame ($\Phi = 1.2$), simulated CH profile is upstream of the experimental one and post-flame velocity is overpredicted, consistent with an overprediction of strained-flame speed.

Results for methane-air flames over a range of equivalence ratios are presented in Fig. 6. In an attempt to reduce the number of parameters varied between experiments, strong burning flames ($\Phi = 1.0, 1.1$) are diluted with excess nitrogen to maintain an approximately constant flame temperature (Zhu et al. 1988). This permits a similar strain-field to be established as equivalence ratio is varied, allowing some decoupling of the various effects. We note reasonable agreement for near-stoichiometric flames ($\Phi = 0.9, 1.0$), but disagreement for both lean and rich flames, with a scaled error between measured and predicted CH-peak locations that varies from 3 to 8 δ_{CH} (cf., Fig. 6a).

Figure 6b compares experimental and simulated CH-profile thicknesses, referenced to the $\Phi = 0.9$ flame. Measured CH-profile thickness is calculated as an ensemble average of the FWHM of individual Gaussian fits to single-shot profiles (60-column average over the flat, central portion of the flame). For the undiluted, $\Phi = 0.9$, $L/d = 0.8$ flame, the measured CH-profile thickness is approximately twice the simulated value. The Point Spread Function (PSF) of the imaging system and the true CH profile can be represented by Gaussians. Taking the effects of the imaging system Point Spread Function (PSF) into account, the PSF width is systematically applied to study the difference between predicted and measured reference profile thicknesses, as a function of equivalence ratio. Figure 6b plots the mean FWHM calculated from multiple shots ($700 < n \leq 1000$) as well as error bars (one standard deviation). A single pixel maps to 0.046 mm in the flame. Simulations

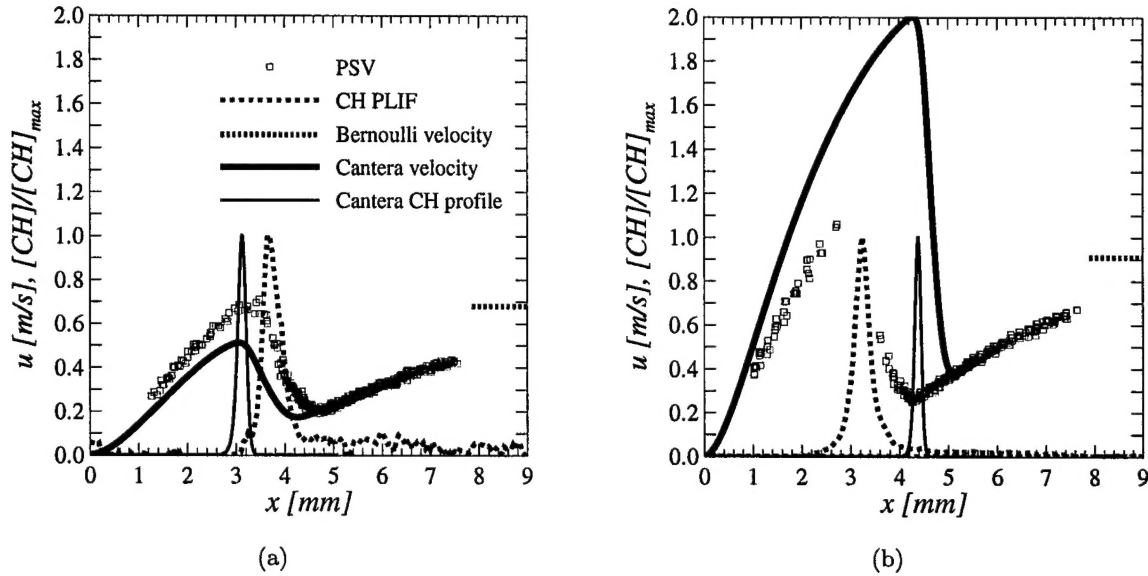


Figure 5: Methane-air flame profiles with simulation boundary at $\ell = 6$ mm. Legend as in Fig. 4(a). (a) $\Phi = 0.63$, $L/d = 0.8$. (b) $\Phi = 1.2$, $L/d = 0.8$.

are seen to underpredict variations in δ_{CH} , both with respect to Φ and dilution. Aspects of this work have been published in Bergthorson and Dimotakis (2003) and Bergthorson et al. (2004).

Preliminary extinction strain-rate measurements against room-temperature stagnation plates have also been made for methane- and ethane-air flames. Extinction is induced through a gradual increase in jet velocity as a sufficiently high framing sequence is recorded. Extinction conditions are derived from the last frame that captures a flame in each sequence. Error estimates derive from ensemble statistics (repeated experiments), or slope-error estimates from a single run, depending on individual image-data and streak suitability. Smooth curves are least-squares fits to the data. Figure 7 gives the results for (undiluted) methane-air and ethane-air flames.

Current investigations aim at locating the source(s) of discrepancies between model and experiment in the strained flame studies. Work presently in progress (AFOSR Grant No. FA9550-04-1-0020) focuses on extensions to a large range of imposed strain rates and a refinement of methane-air extinction strain-rates measurements, with plans for other fuel-air mixtures relevant to SCRAM-JET combustion. Specifically, following the methane-air baseline experiments, ethylene-air flames will be studied, along with flames utilizing other fuel blends. The hydrocarbon flame experimental and simulation work is performed in collaboration with D. Goodwin, as well as the more-detailed simulation work discussed below, and is part of the Ph.D. work of J. Bergthorson.

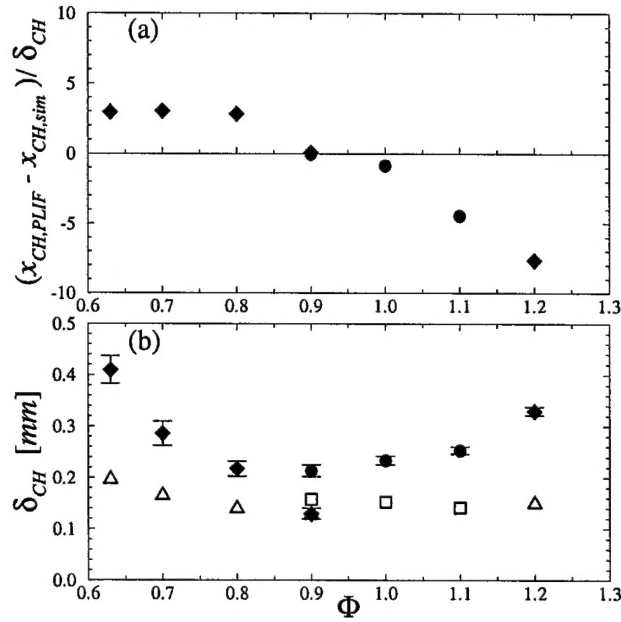


Figure 6: (a) Difference in measured ($x_{CH,PLIF}$) and predicted ($x_{CH,sim}$) peak locations of CH, scaled by the simulated CH profile thickness (δ_{CH}), as a function of equivalence ratio. Undiluted flames marked with diamonds; diluted flames with circles. (b) Experimental and simulated CH profile thicknesses (FWHM). Experimental data is referenced to the $\Phi = 0.9$ undiluted flame. Undiluted flames marked with diamonds (experiment) and triangles (simulation). Diluted flames marked with circles (experiment) and squares (simulation).

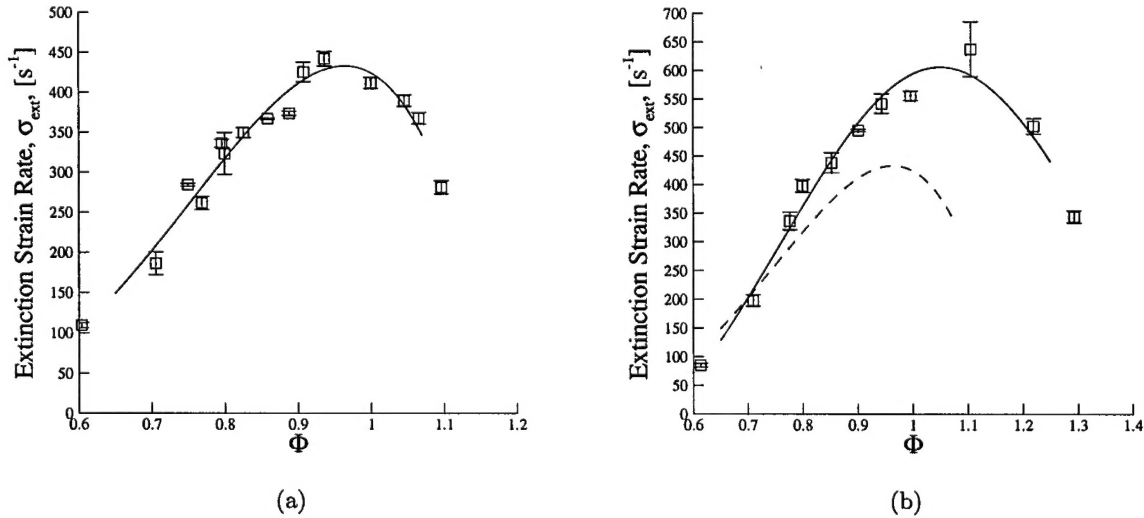


Figure 7: Extinction strain rates against a room-temperature stagnation plate. (a) Methane-air (b) Ethane-air (dashed curve is fit to methane-air data)

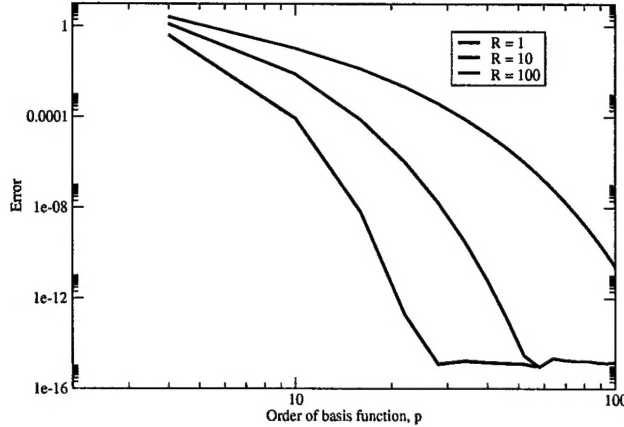


Figure 8: Convergence study of the Helmholtz equation: $\nabla \cdot (\mu \nabla p) + \lambda p = f$ for three different “density ratios”, $R = \max_{\Omega} \mu(x, y) / \min_{\Omega} \mu(x, y)$ where $\mu(x, y) = 1/(a + \sinh(x^2 + y^2))$. p -type (polynomial-order) convergence is studied and illustrated here. h -type (element-size) convergence is also possible.

1.2 Simulations

In an effort parallel to the experiments described above, we have been developing software suitable for the study of stagnation-flow flames in a 2D axisymmetric domain. This is aimed at simulating the full axisymmetric stagnation flow and stabilized flames, with full chemistry and transport models, to elucidate errors in chemistry models through side-by-side comparisons with experiments. The code aims to simulate the entire experiment, including wall-nozzle proximity effects, entrainment effects, and nozzle-curvature effects. The code is based on the spectral-element method, which was chosen for its high-accuracy and ability to handle complex geometries. The method also has an advantage in controlling numerical simulation errors, owing to convergence properties common to spectral methods. To date, the method has typically been used for the simulation of incompressible flows, with limited application to variable-density and reactive flows (Tomboulides et al. 1997).

The simulation relies on a low Mach number approximation of the compressible Navier-Stokes equations, as used in Day and Bell (2000), for example. One of the major differences between the incompressible (zero Mach number limit) and compressible equations is that the latter have a non-constant factor in the Pressure Poisson Equation (PPE), and the viscous and diffusion terms in the momentum equation. Our implementation of the spectral-element method accommodates this difficulty. The convergence study also shows that spectral convergence is achieved, as depicted in Fig. 8.

This method works for a sufficiently large variation of μ , which could represent either transport properties (such as viscosity), or the reciprocal of density in this formulation, whose ratio is the order of 10. In the present work, we use a single-step reaction model:



Reaction rate parameters for the Arrhenius form are taken from Westbrook and Dryer (1981). Figure 9 shows an instantaneous snapshot of the temperature and combustion product fields, at a time step that is intermediate between ignition and steady state. Improving the numerical efficiency of the code is an issue being addressed at this time. The results have not been integrated

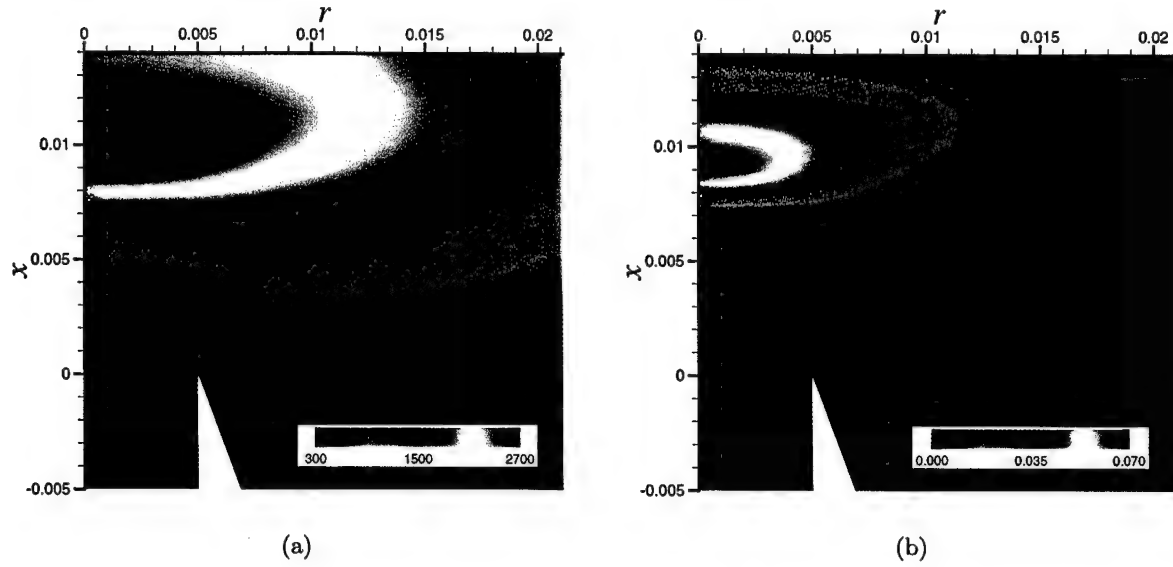


Figure 9: (a) Temperature field. (b) Water product concentration field.

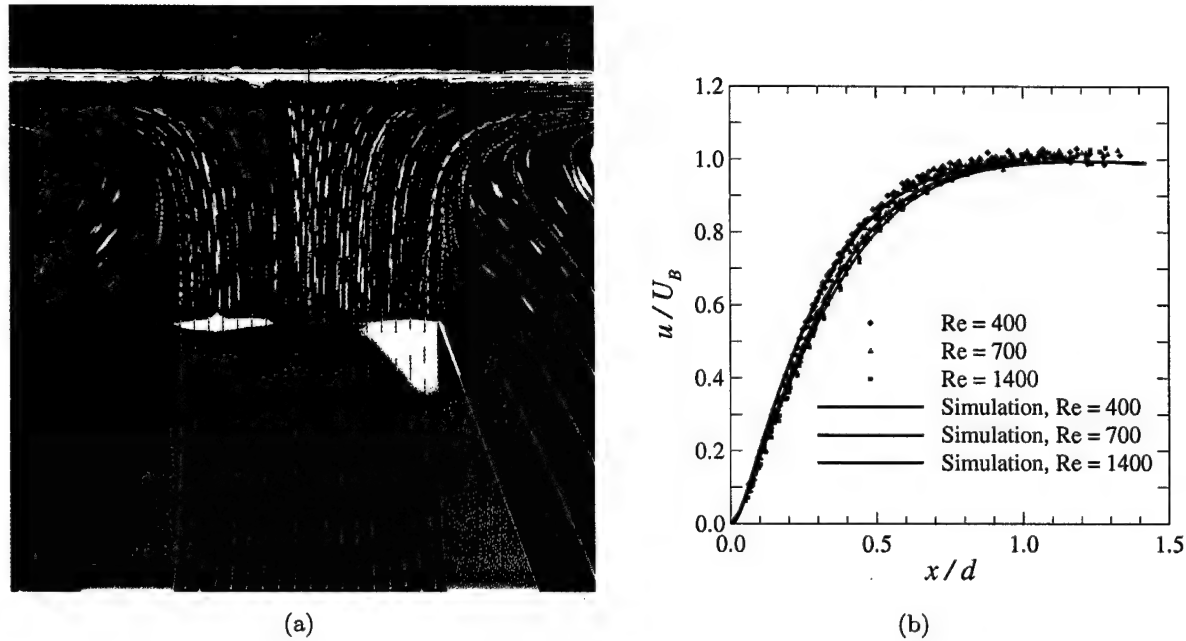


Figure 10: (a) Particle streak image detailing entrained flow with superimposed axisymmetric viscous calculation (yellow lines). $Re = 700$, $L/d = 1.0$. (b) Comparison of calculated velocity profiles to experimental (PSV) data detailing Reynolds number effects.

to steady state. The results do illustrate, however, the applicability of the simulation methodology to stagnation-flow flames.

Simulations of cold impinging jet flow were completed and compared with experimental results. These simulations provide insight into the hydrodynamics of the flow in which stagnation flames are stabilized. The unsteady Navier-Stokes equations are integrated in time from a quiescent state until a steady-state flow is attained. In these simulations, 10th- to 12th-order polynomials are used

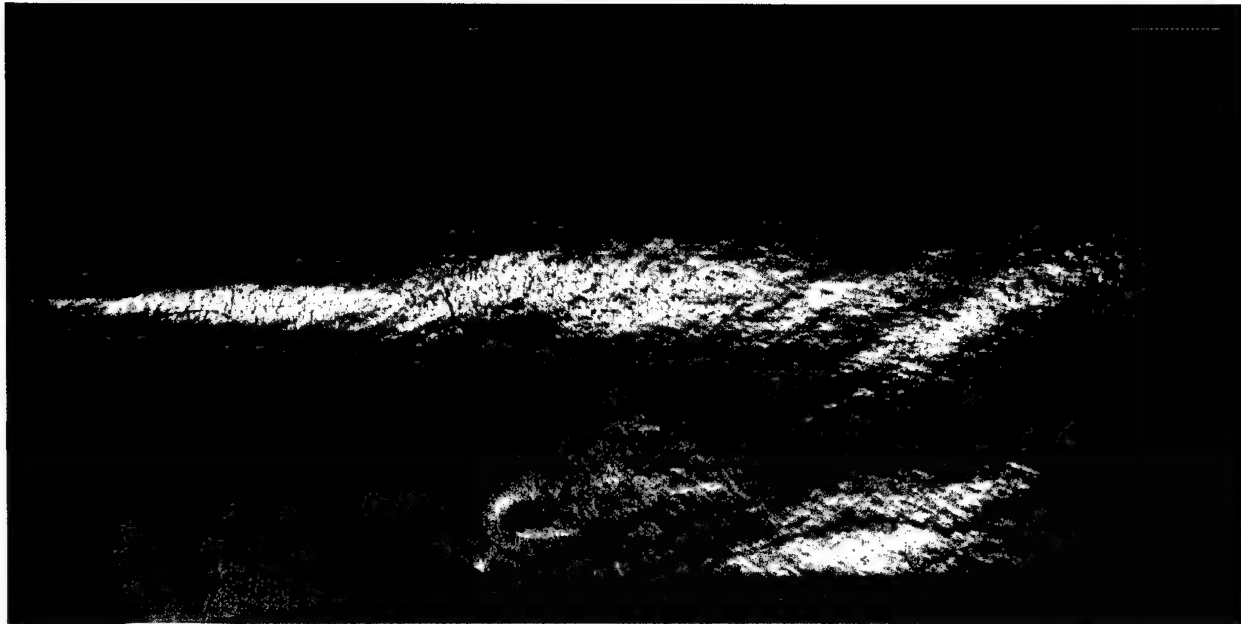


Figure 11: Schlieren visualization of subsonic flow with ramp injection. $U_1 \simeq 120$ m/s: 1.0% H_2 , 0.25% NO, 98.75% N_2 (upper stream). $U_2 \simeq 11$ m/s: 1.0% F_2 , 99.00% N_2 (lower stream).

as an expansion basis in each element, depending on geometry. These choices provide a balance between solution accuracy and computational time.

Figure 10(a) compares particle-streak-image experimental (PSV) data and streamlines from the axisymmetric viscous simulations. Good agreement can be seen, even in the entrainment region where velocities are very low ($< 0.02 U_B$). Figure 10(b) compares the experimental data with the axisymmetric viscous calculations at $L/d = 1.4$ and $Re = 400, 700$, and 1400 . Differences between experimental and numerical results for these three cases are less than $0.015 U_B$ root-mean-square (rms), confirming that the choice of inflow/outflow boundary conditions in the simulations is adequate.

This part of the effort was performed in collaboration with D. Meiron, was cofunded by the Caltech DOE/ASCI Alliance Center, and is part of the Ph.D. research of K. Sone.

2 Mixing and combustion in complex high-speed flows

2.1 Experiments

Experiments were performed to investigate the aerodynamic control of internal flows, as occur, for example, in subsonic diffusers and scramjet combustors. With aerodynamic control, it is possible to realize the benefits of variable geometry control, without the penalties of added weight and mechanical complexity.

Figure 11 shows a schlieren visualization of the flow field under investigation. In this image, the upper-stream flow enters the test section at a speed of $U_1 \simeq 120$ m/s and the lower-stream flow is injected through an inclined perforated plate at a (test-section lower-speed stream) speed of $U_2 \simeq 11$ m/s. The schlieren visualization in these data is made possible by the temperature rise owing to the heat release in the reaction between dilute hydrogen (H_2) premixed with nitric oxide (NO) in the upper stream, and dilute fluorine (F_2) in the lower stream. Initially, a shear layer

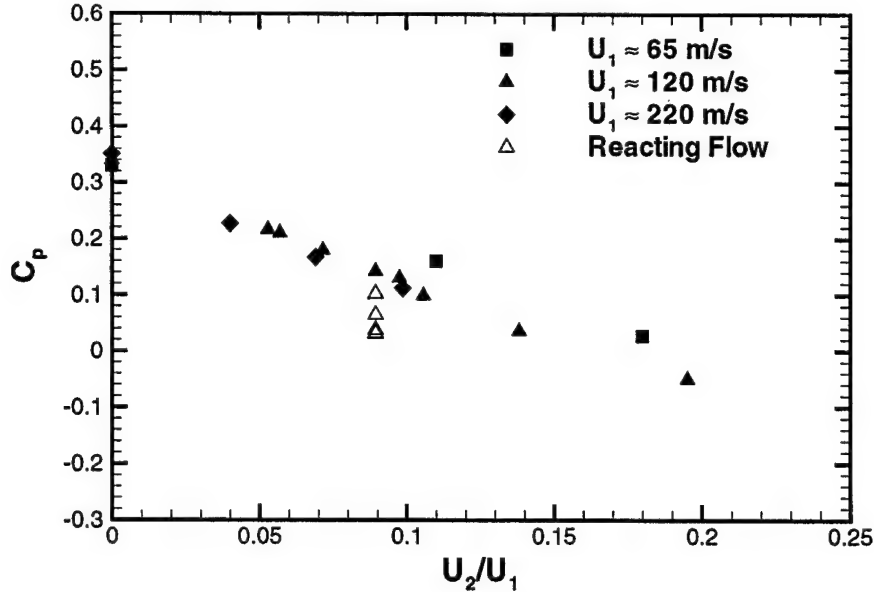


Figure 12: Overall pressure coefficient as a function of injection velocity ratio. Points for reacting flow correspond to concentrations of H_2 and F_2 , from top to bottom, of 1, 2, 4 and 6%, and $U_1 = 123$ m/s.

is formed between the upper- and lower-stream reactants, with a small pocket of unmixed lower-stream fluid visible immediately downstream of the inclined injection plate. Further downstream a secondary mixing zone is visible where recirculated hot products mix with fresh reactants. This secondary mixing zone, where strain rates are significantly lower compared to the primary shear layer, and where hot recirculating products are available to keep a flame lit, is promising for use in scramjet combustors.

An important quantity in these flows is the overall pressure coefficient,

$$C_p = \frac{p_e - p_i}{\frac{1}{2}\rho_1 U_1^2} \quad (4)$$

where p_e and p_i are the (upper-guidewall) pressure at the test section exit and inlet, and U_1 is the upper-stream inlet velocity. Figure 12 plots the overall pressure coefficient as a function of the injection velocity ratio, U_2/U_1 , for three different inlet velocities. As can be seen, the flow can be controlled from a fully stalled diffuser to a near-classical free shear layer, with negligible streamwise pressure gradient, by varying the injected mass flux (lower-stream flow). There is a slight increase in control authority as the inlet velocity, U_1 , is increased. At higher inlet velocities, the injected mass flux ratio required to achieve the same overall pressure coefficient, is lower.

A series of experiments was conducted to investigate the effects of heat release on this flow-field. Similar control over the flow-field is possible, by varying the level of heat release, while holding the injected mass flux constant. The overall pressure coefficient for these experiments is also plotted in Fig. 12. With reacting flow, there is a further benefit from the combustion-induced dilatation. Requirements for mass injection at the highest heat-release level are reduced by almost a factor of two. Specifically, only half as much mass injection is required to achieve the same overall pressure coefficient performance, with dilatation from the exothermic chemical reaction playing the same role as added mass flux.

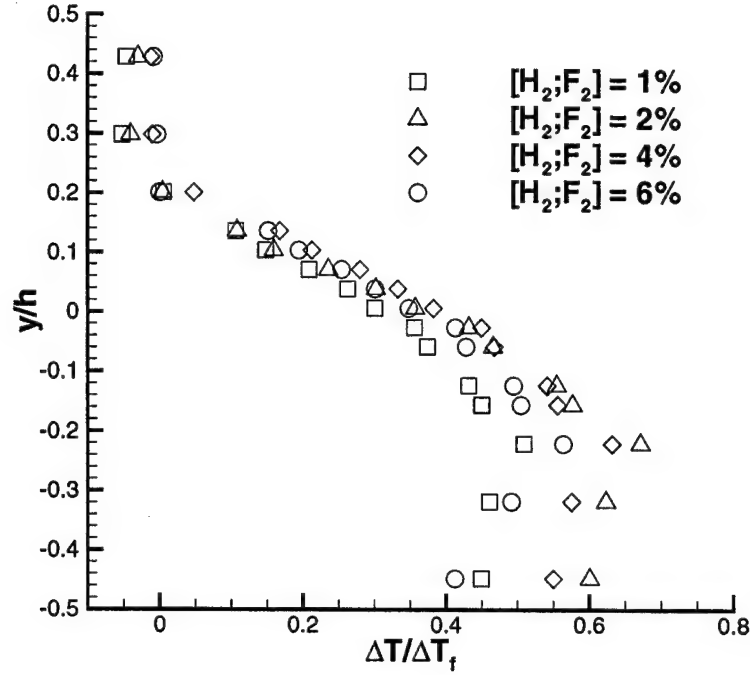


Figure 13: Normalized temperature rise profiles for increasing levels of heat release.

As documented in Hermanson et al. (1987) and Hermanson and Dimotakis (1989), overall entrainment into a shear layer decreases with increasing heat release. Figure 13 plots the normalized temperature rise with increasing heat release, achieved by increasing the concentration of H_2 and F_2 in the upper and lower streams, respectively. It is seen that the benefits of the recirculation zone and the peak temperature rise peak at $[H_2;F_2] = 2\%$. At higher concentrations, even though heat release is higher, the reduction in entrainment extends the recirculation zone past the measuring station, and the level of mixing, as measured there, decreases. Flow acceleration owing to the displacement (dilatation) effect from the reaction is illustrated in Fig. 14. As the heat release is increased, so are exhaust velocities, and thrust.

Using a model proposed by Dimotakis (1991), the mean density reduction in a shear layer can be related to the mixed-fluid and product fractions,

$$\frac{\Delta\rho}{\rho_0} \approx \frac{\left(\frac{\delta_P}{\delta}\right) \frac{\Delta T_f}{T_0}}{1 + \left(\frac{\delta_P}{\delta_m}\right) \frac{\Delta T_f}{T_0}} \quad (5)$$

Fitting data for the current experimental geometry to this expression, we calculate values of $\delta_m/\delta = 0.74$ and $\delta_P/\delta_m = 0.48$, compared to values of $\delta_m/\delta = 0.63$ and $\delta_P/\delta_m = 0.5$ for classical free shear layers. Thus, the mixed-fluid fraction is estimated to be $\sim 20\%$ higher in the flow with ramp injection, versus a classical free shear layer.

Preliminary experiments have been conducted to investigate the behaviour of the flow in this geometry, with a supersonic inflow. Figure 16 is a schlieren visualization of the flow for $M_1 \sim 1.02$. Expanding slightly over the ramp, the flow initially accelerates to $M \sim 1.05$. As in the subsonic visualization (Fig. 11), a pocket of pure injected fluid is visible just downstream of the ramp.

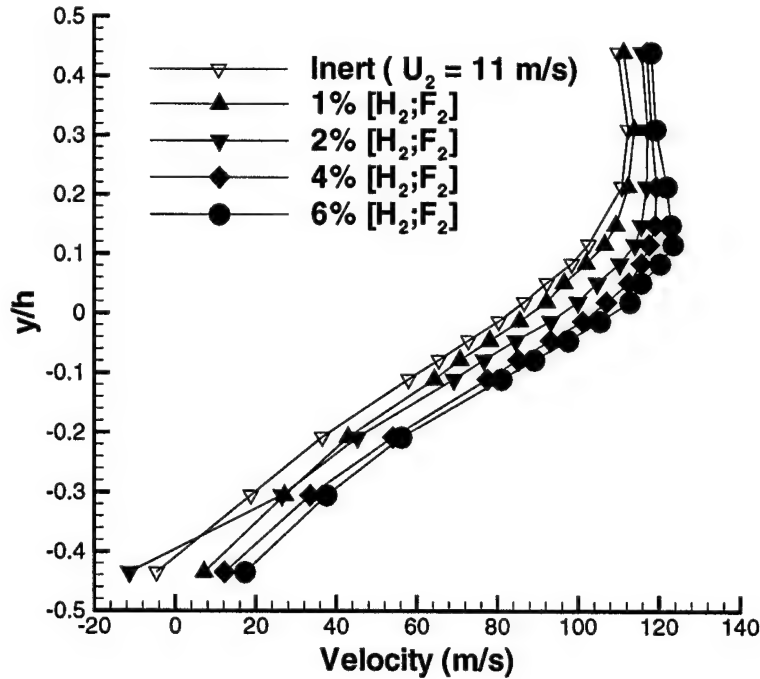


Figure 14: Test section-exit velocity profiles with increasing heat release.

The recirculation zone extends further downstream, all the way to the test section exit. For this flow, measured upper-guidewall static pressures are in accord with those estimated from Mach numbers based on the flow-visualization data. Importantly, upper-streamtube area estimated from upper-guidewall pressure data agrees well with the visual shear-layer thickness, assuming negligible entropy production, *i.e.*, negligible total-pressure losses.

Work currently in progress relies on, so-called, “flip” experiments (Mungal and Dimotakis 1984), at several Reynolds numbers, to provide direct measurements of the probability and flux of mixed fluid exiting the test section.

This part of the effort is part of the graduate research of M. Johnson and E. Iglesias and is performed in collaboration with G. Katzenstein, E. Dahl, and D. Lang.

2.2 Simulations

A parallel computational effort seeks to simulate high-speed, turbulent reacting flows, in general, and the flow studied experimentally in the section above, in particular. The goal in this part of the effort has been to simulate the experiments conducted in the GALCIT S³L facility by M. Johnson and E. Iglesias (Sec. 2.1). In the particular case of interest, the top stream is slightly supersonic, with $M = 1.05$, and the lower is subsonic, with a mass flux $\dot{m}_2 \sim 0.16$ kg/s. This corresponds to a mass-flux ratio between the two streams of $\dot{m}_1/\dot{m}_2 \sim 20$.

At this stage, the simulations rely on a simple model based on the two-dimensional Euler equations for the flow of a single species. The energy equation is that for the total energy. The perfect-gas equation of state is used to close the system. The gas in the simulations is assumed to be nitrogen, for which $\gamma = 1.4$.

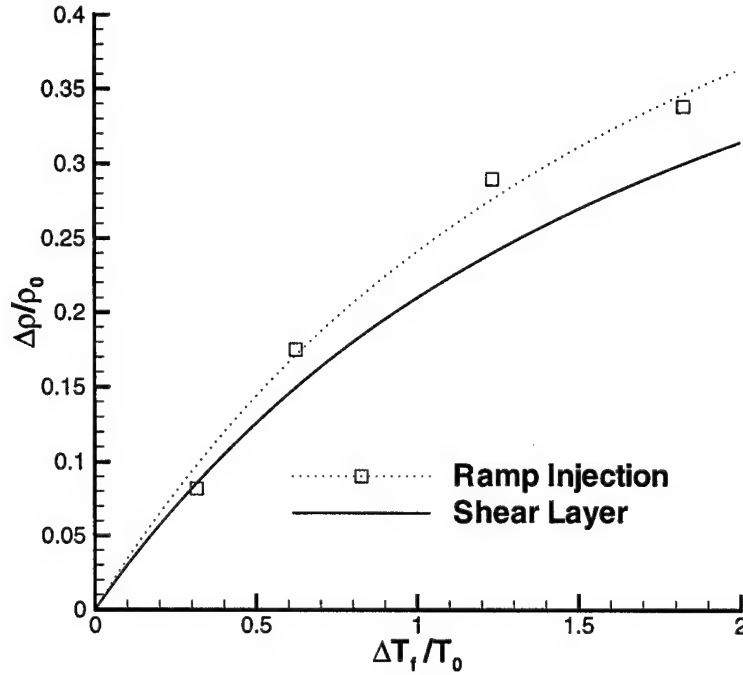


Figure 15: Mean density reduction vs. adiabatic flame temperature rise.

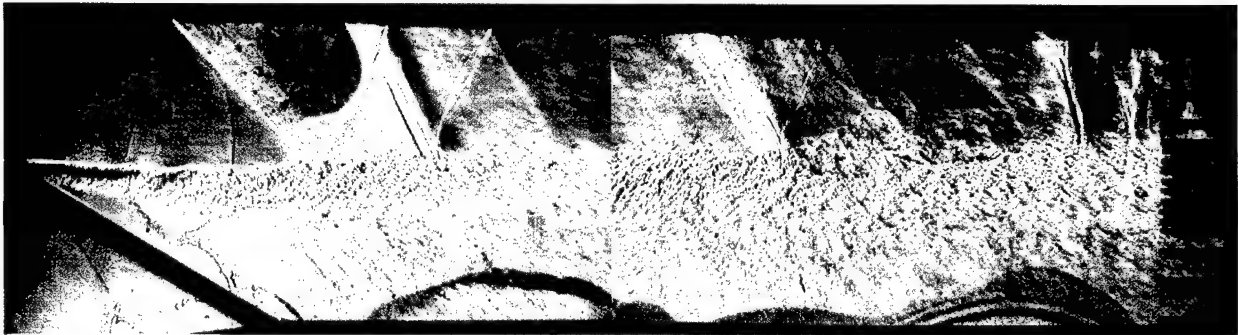


Figure 16: Schlieren visualization of supersonic flow with ramp injection. Incoming Mach number $M_1 \sim 1.02$.

A finite-volume shock-capturing numerical method is used. We are using a MUSCL-Hancock scheme that is second-order in space and time (van Leer 1984). An exact Riemann solver is used to calculate the numerical flux (Godunov 1959).

A boundary-fitted grid with ghost cells at the boundary is used. Boundary conditions are applied by selecting the appropriate values of the solution vector in the ghost cells. A characteristic boundary condition is used for the inlet and a zero-gradient normal to the boundary condition is used at the downstream boundary (the value of the last cell is copied in the downstream ghost cells). At this writing, boundary conditions are being upgraded to better-capture outflow details. A main difficulty in these simulations is to capture the reentrant jet (flow moving from downstream to upstream) observed in the experiments near the lower guide wall. That would not have been

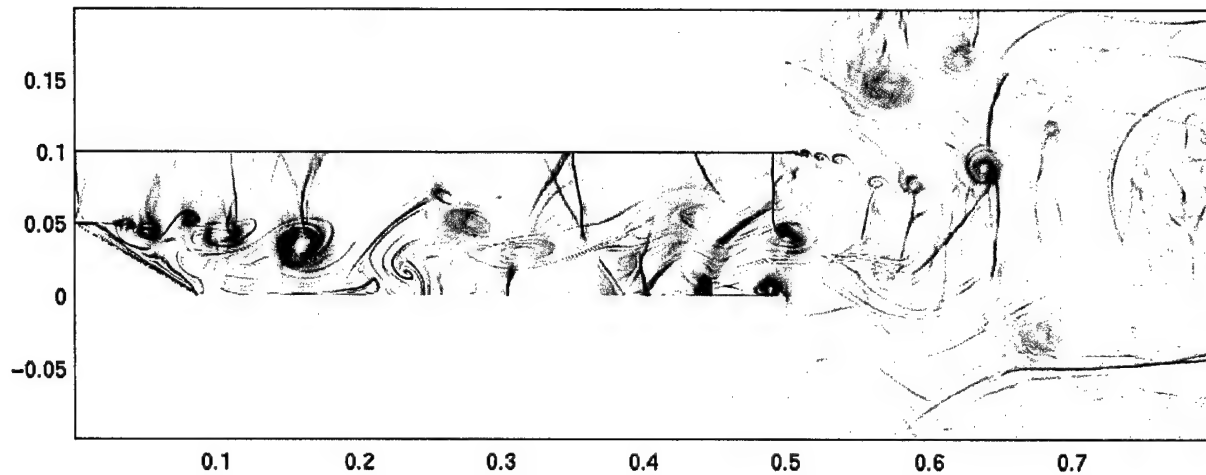


Figure 17: Schlieren of the computed instantaneous density field.

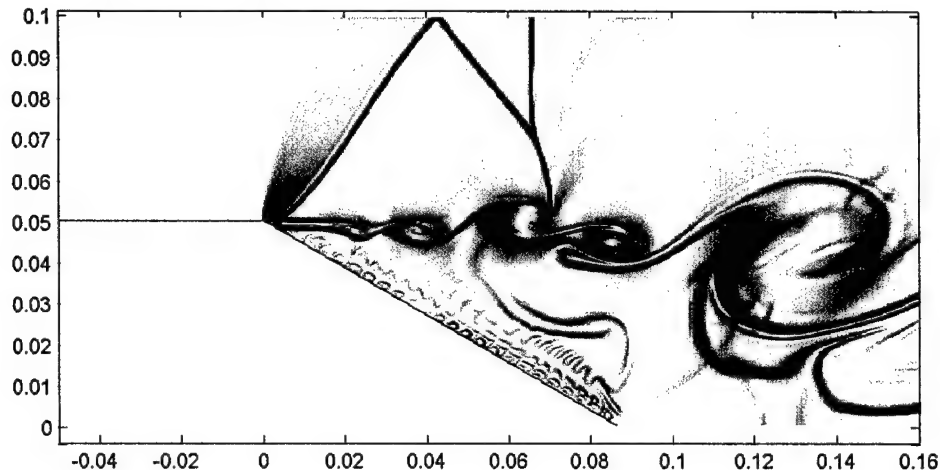


Figure 18: Schlieren of the computed instantaneous density field. For a simulated ramp geometry that is a closer approximation to the experiment, oblique waves are observed at the inlet.

possible without the use of a downstream “box” (Fig. 17).

Figure 17 shows an instantaneous schlieren visualization of the computed density field. The shear layer develops from the initial Kelvin-Helmholtz instability within a short distance downstream of the inlet. Complicated shock structures form in the top supersonic stream. With a more-detailed representation of the inlet geometry (Fig. 18), oblique waves observed in the experiments are also captured in the simulations. In Fig. 18, the top-stream inlet has been moved somewhat upstream, the top part of the ramp is closed, and the ramp is no longer modeled as a uniform-inflow boundary, but represented in terms of “open” (inflow) and “closed” (wall) portions, *i.e.*, a perforated wall (in 2D), as in the (3D) experiments. The ramp inflow conditions are adjusted to match the experimentally set low-speed stream mass flux. Every incremental change implemented in the simulations that better captured experimental conditions, brought simulation and experiment closer together. Figure 19 shows a comparison of total-pressure profiles at the exit of the test section ($x = 0.36$ m). The computed and measured total pressure profiles are in

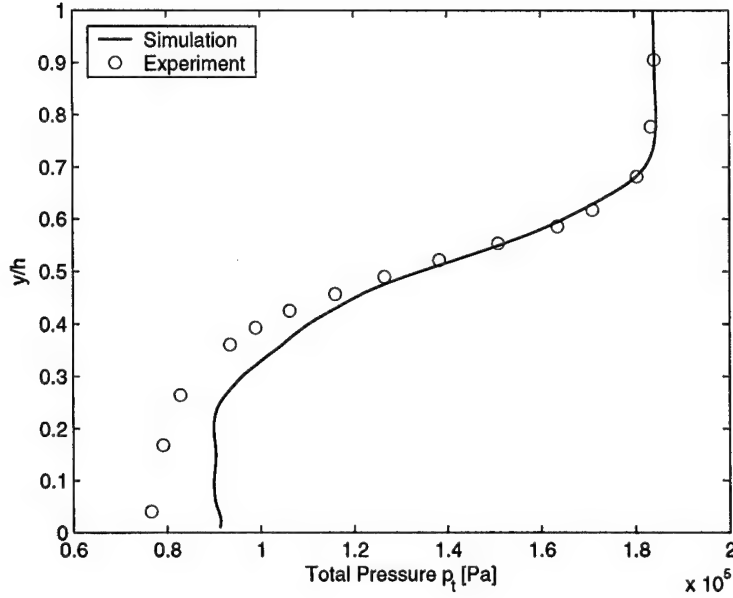


Figure 19: Comparison of the exit ($x = 0.36$ m) total-pressure profiles. Simulation (solid line) and experimental measurements (circles) are in accord in the upper half of the duct.

accord in the top part of the duct. In this region, there is no reverse flow and the experimentally measured pitot pressures represent a reliable estimate of local total (stagnation) pressures. In contrast, near the lower guidewall, the flow is reentrant and the (forward-facing) pitot-probe measurements are unreliable. Simulations are also difficult in this region, with the dynamics responsible for the reentrant jet in the experiment and in the simulation arising for different reasons. This represents a modeling challenge that will be addressed in the future, exploiting theoretical and numerical-simulation advances in compressible-turbulence modeling developed as part of the Caltech DOE/ASCI Alliance program.

This work was performed in collaboration with Carlos Pantano and Ralf Deiterding, with some support from the Caltech DOE/ASCI program, and is part of the Ph.D. research of Georgios Matheou.

3 Rayleigh-Taylor Instability

Rayleigh-Taylor (RT) instability occurs when fluids of different density are subject to an acceleration with a component opposite in direction to the density gradient. The canonical flow configuration studied consists of high-density fluid atop low-density fluid, subject to gravity. More generally, and of more immediate interest in the context of mixing in high-speed and accelerating flows, RT instability also occurs when variable-density fluid (such as that produced by combustion) is subject to a Lagrangian acceleration in a turbulent flow, for example. Driven by local buoyancy forces, initial density-field perturbations grow to finite amplitude, eventually forming plumes of rising low-density fluid (bubbles) and descending high-density fluid (spikes). These structures merge and interact, forming larger scales, but also develop secondary Kelvin-Helmholtz instabilities, generating smaller scales. If these are allowed to develop, the flow eventually becomes turbulent. Our analysis and simulations have focused on the effect of density ratio on RT instability of miscible fluids. Many previous experiments and simulations use immiscible fluids, are restricted to moderate density ratios, or employ grid-dependent numerical diffusion as a surrogate sub-grid turbulence model.

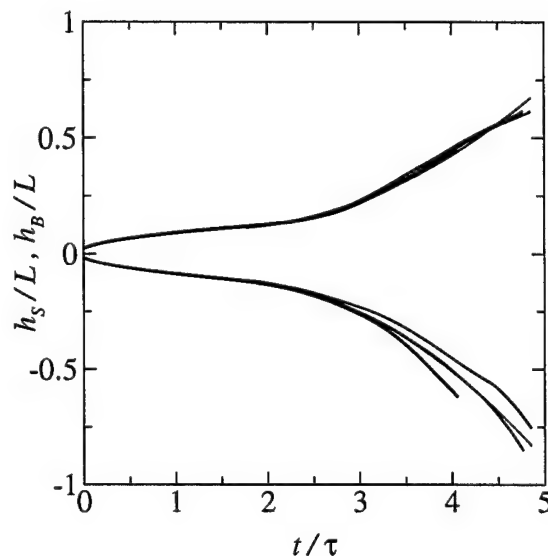


Figure 20: DNS bubble and spike penetrations for $\mathcal{A} = 1/4$ (blue), $1/2$ (green), and $3/4$ (red). L is the width of the computational domain, $\tau = \sqrt{L/\mathcal{A}g}$, $h_b > 0$, and $h_s < 0$.

Three direct numerical simulations (DNS) of RT instability, at density ratios of $\rho_2/\rho_1 = 5/3$, 3, and 7 have been completed. Here, ρ_2 and ρ_1 are the heavy- and light-fluid densities, respectively. In these simulations, all relevant spatial and temporal scales are resolved. The parameters for these simulations were carefully chosen to minimize differences due to initial conditions, an issue identified in an earlier simulation (Cook and Dimotakis 2001). The grid resolution of $256 \times 256 \times 1024$ restricted final Reynolds numbers (based on mixing zone width and growth rate) to between 2000 and 4000, depending on the density ratio. The simulations were run on the Advanced Scientific Computing (ASC) supercomputers at Lawrence Livermore National Laboratory, using a code developed by A. W. Cook and modified by us to enable higher-density-ratio simulations ($\rho_2/\rho_1 > 4$). The principal results of these simulations are:

1. Scaling time by $\tau \equiv \sqrt{L/\mathcal{A}g}$, where L is the RT-flow spatial extent,

$$\mathcal{A} \equiv \frac{\rho_2 - \rho_1}{\rho_2 + \rho_1} \quad (6)$$

is the Atwood number, and g the acceleration magnitude, approximately collapses the bubble penetration, h_b , with a relatively weak residual Atwood number dependence persisting for the spike penetration, h_s . As observed in experiments with immiscible fluids, and simulations using the Euler equations, bubble and spike penetrations become increasingly asymmetric with increasing Atwood number. See Fig. 20.

2. The bubble/drop terminal velocity (Davies and Taylor 1950; Batchelor 1967),

$$U = c \sqrt{\frac{\Delta\rho}{\rho} g R}, \quad (7)$$

where $\Delta\rho$ is the density difference across the bubble and spike, ρ is the density of the ambient fluid into which the bubble/spike is advancing, g the acceleration, R the radius of curvature, and c a geometry-dependent constant, correctly accounts for the Atwood number dependence of the individual bubble and spike velocities (Fig. 21). With additional mass- and energy-conservation constraints, Eq. 7 can be used to construct a model of RT growth for arbitrary density ratio.

3. Asymmetric bubble and spike growth is correlated with asymmetric volume-averaged mixed-fluid composition (Fig. 22).

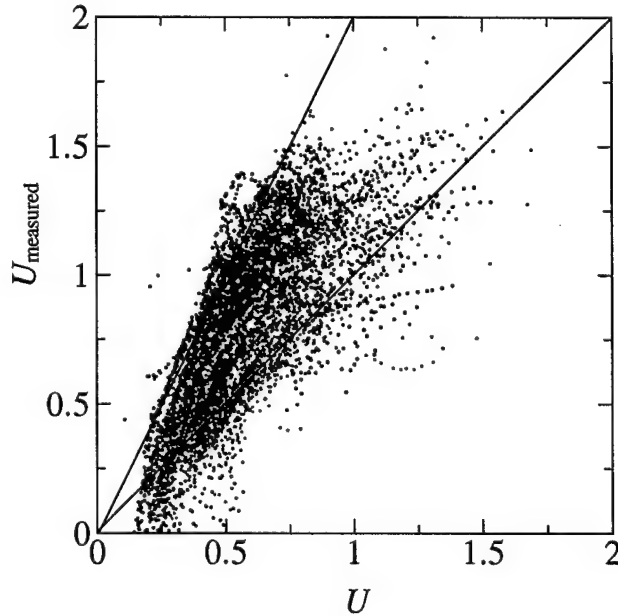


Figure 21: Scatter plot of measured bubble and spike velocity versus Eq. 7 for $\mathcal{A} = 1/4$ (blue), $1/2$ (green), and $3/4$ (red). For each structure, $\Delta\rho$, ρ , and R are extracted from the DNS data and used to compute U with $c = 2/3$. Unbroken black lines are drawn with gradient 1 and 2 for reference.

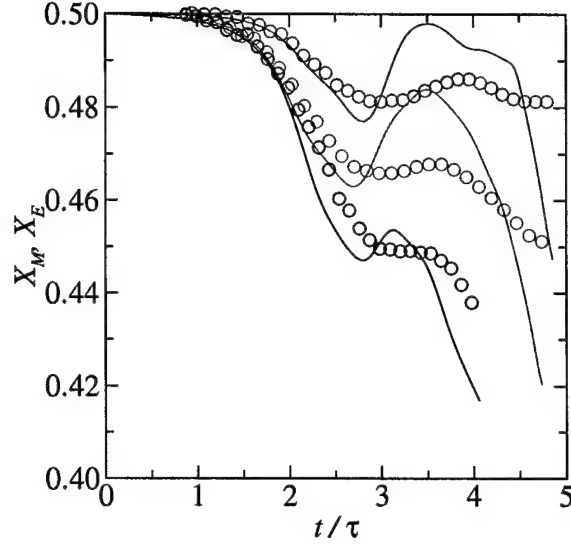


Figure 22: Measured volume-averaged mixed-fluid composition, X_m (lines), compared with calculated homogeneously-mixed entrained-fluid composition, $X_E = E/(1 + E)$ (symbols), for $\mathcal{A} = 1/4$ (blue), $1/2$ (green), and $3/4$ (red). $E = h_b/h_s$ is the entrainment ratio.

The DNS do not achieve self-similarity. For self-similar flow in the limit of infinite Reynolds and Peclet numbers, dimensional analysis predicts,

$$h_{b,s} = f \left(\frac{\rho_2}{\rho_1} \right) g t^2 \quad (8)$$

where g is the acceleration, and t is time. In the literature, this is usually expressed as,

$$h_{b,s} = \alpha_{b,s} \mathcal{A} g t^2, \quad (9)$$

where $\alpha_{b,s}$ are Atwood-number-dependent coefficients.

Large eddy simulations (LES) of RT instability at three density ratios of $\rho_2/\rho_1 = 5/3$, 3, and 7 were also completed. In these simulations, the most energetic scales are resolved and subgrid-scale (SGS) quantities are modeled using the stretched-vortex model (Misra and Pullin 1997; Voekl et al. 2000; Pullin 2000). In addition to the SGS model, compact and spectral filters are used to remove energy from subgrid wavenumbers. Two sets of simulations were performed.

In the first set, coarse ($64 \times 64 \times 256$)-grid simulations corresponding to the fully resolved DNS were performed. The LES was initialized using the filtered DNS data, allowing a direct comparison between the DNS and LES. The principal results are:

1. Large-scale features, such as bubble and spike penetration (Fig. 23) and resolved-scale spectra are preserved by the model.
2. In these comparisons, resolved-scale dissipation dominates subgrid dissipation. Comparisons with higher Reynolds number experiments or DNS are needed for a more definitive test of model validity.

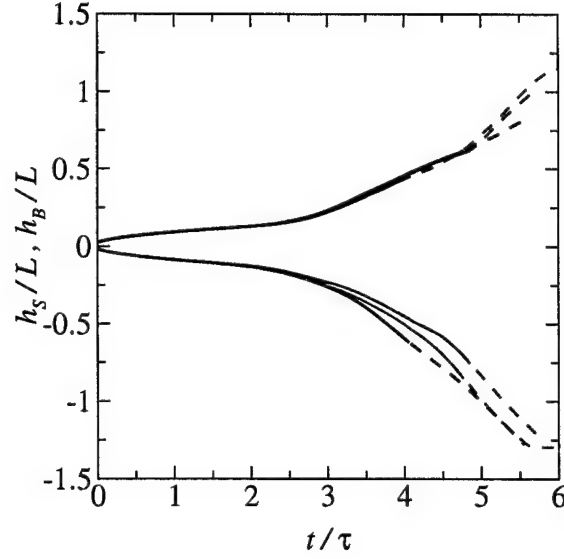


Figure 23: DNS (unbroken lines) and LES (broken lines) bubble and spike penetrations for $\mathcal{A} = 1/4$ (blue), $1/2$ (green), and $3/4$ (red).

In the second set, $(128 \times 128 \times 256)$ -grid simulations were performed to obtain model predictions of RT flow at final Reynolds numbers in excess of 50,000. In these simulations, subgrid dissipation dominates resolved-scale dissipation, but resolved-scale kinetic energy dominates subgrid kinetic energy. The principal results are:

1. Mole-fraction profiles collapse and quadratic mixing zone growth is obtained (Fig. 24), suggesting approximate self-similarity.
2. Kolmogorov scaling ($k^{-5/3}$) of the resolved-scale kinetic energy spectrum is observed (Fig. 25). The scalar energy decays somewhat faster at high wavenumbers, consistent with results from application of the stretched-vortex mixing model to passive scalar mixing in homogeneous isotropic turbulence (Pullin 2000).

In both simulation sets, ‘unphysical’ scalar excursions are observed. These scalar excursions occupy a small volume fraction and appear to average out in the statistics, but limit the density ratio at which the LES can be run.

Preliminary results from the LES-SGS analysis of the RT flows were presented at the Caltech LES-SGS conference (Mattner and Dimotakis 2003). An update has been accepted for presentation in the upcoming meeting on mixing in compressible turbulent flows (Mattner et al. 2004).

This part of the work was performed by Trent Mattner and undertaken in collaboration with A. W. Cook and P. L. Miller of the Lawrence Livermore National Laboratory, and D. Pullin, under the auspices of the US Department of Energy by the U.C. Lawrence Livermore National Laboratory, under Contract No. W-7405-Eng-48, and by the Caltech DOE/ASCI Alliance Center, subcontract B341492.

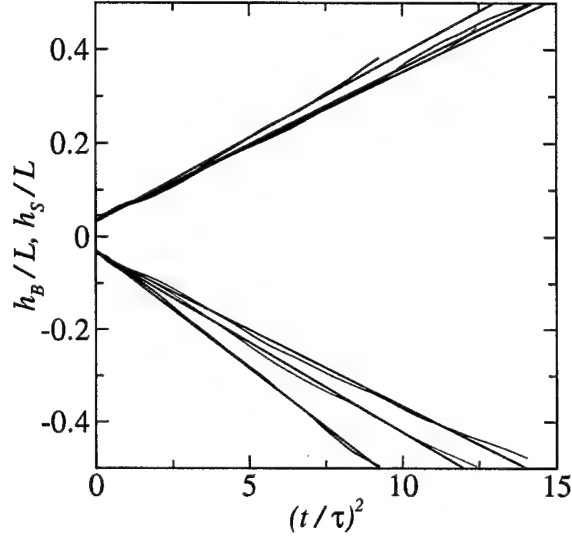


Figure 24: Bubble and spike penetrations from high Reynolds number LES for $\mathcal{A} = 1/4$ (blue), $1/2$ (green), and $3/4$ (red).

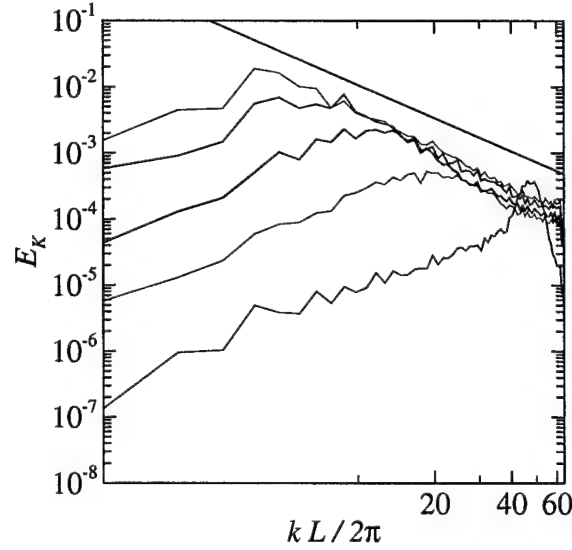


Figure 25: Temporal development of kinetic energy spectra from high Reynolds number LES at $\mathcal{A} = 1/2$. The black line has a slope of $-5/3$.

4 Advances in high-speed digital imaging and data acquisition

The digital-imaging and high-speed data-acquisition part of this effort has mostly focused on hardware development, with software/firmware developments on an as-necessary basis.

4.1 KFS camera data-acquisition system

The KFS camera system is a camera system designed for high-speed low-noise image acquisition. The KFS camera CCD image sensor was designed by Mark Wadsworth of JPL. It has a resolution of 1024×1024 pixels, with 32 output channels, to acquire up to 1000 images per second. The KFS camera head electronics were designed by Daniel Lang with assistance from Steve Kaye. The original camera head housing was designed by Pavel Svitek. The KFS camera system includes a VXI bus enclosure with 8 4-channel A/D converter boards (VXIADC2), for a total of 32 channels, a VXI timing board (VXITIM2), a VXI power board (VXICAM2), and a control PC (Fig. 26).

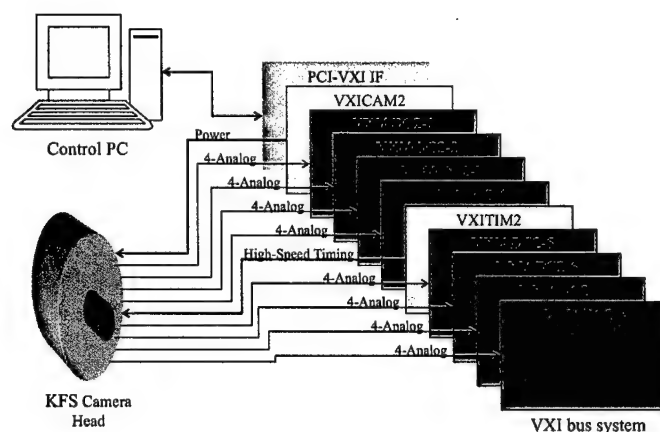


Figure 26: KFS camera data-acquisition system

At this time, the KFS CCD image sensor and data acquisition system relies on a 1024×1024 CCD with 32 output channels at 40 MHz, for up to 1000 fps (frames/second). The system has been tested to 333 fps (current lasers limit us to 200 fps; 8 VXIADC2 boards are operating, with 4 12-bit A/D converters and 512 MB memory for 4 GB total memory; the system can acquire 2700 contiguous frames (12-bit packed), or 4000 to 8000 contiguous frames with lossless compression; and an auxiliary data port is provided on each A/D board for future disk-storage and faster data-acquisition expansions.

4.2 KFS camera noise reduction

The KFS data-acquisition system has been completed and is working well. Low-light level applications, however, as encountered in its use in gas-phase imaging or at the Palomar observatory, can benefit from improved noise figures. The plot below shows the original noise figures (1024×1024) and original binned noise figures (binned to 512×512) in electrons/pixel.

A new VXI enclosure was installed with a separate low-noise power supply for the analog circuits. Also, the analog inputs on the VXI A/D converter boards were adjusted to maximize

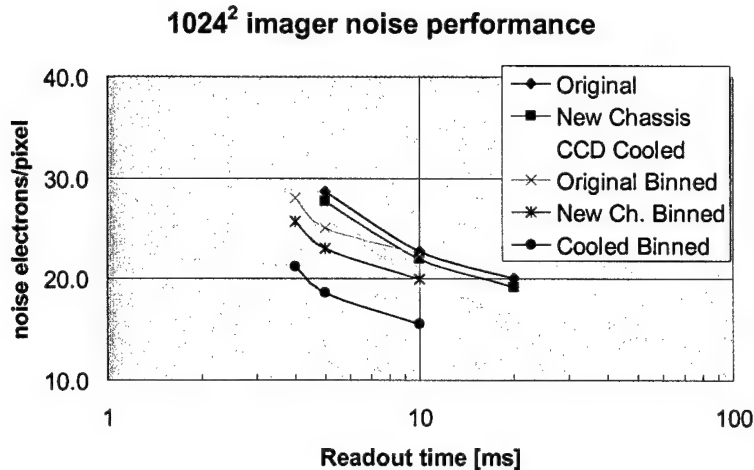


Figure 27: KFS camera noise performance

the Common Mode Rejection Ratio (CMRR). The resulting improved noise figures are shown on the “New Chassis” and “New Ch. Binned” graphs in Fig. 27. Finally, the CCD camera head was connected to the outer vacuum jacket of a liquid nitrogen dewar and the assembly was evacuated. A cold finger provides a thermally conducting path between the inner vacuum jacket of the dewar and the rear of the CCD. The liquid nitrogen cools the CCD down to an operational temperature of -38°C . The cold finger and the mounting adapter between the dewar and the camera were designed by Brian Kern. The final improved noise figures are shown on the “CCD Cooled” and “Cooled Binned” graphs in Fig. 27.

4.3 New KFS/HIT camera head design

A problem encountered with evacuating the camera and cooling the CCD is that vacuum grease and heat sink grease evaporates from the warmer surfaces and condenses on the coldest item, the CCD image sensor itself. Another problem is that the shutter deposits small dust particles on the surface of the CCD. This has led to a redesign of the camera head to minimize these problems and simplify manufacture of the camera head. The new design places the shutter in front of the optical window and the power board at the rear of the camera leaving only the CCD board inside the evacuated enclosure. The new design reduces the number of hermetic connectors from 34 to 4 (the 32 coaxial video connectors are replaced by two 50-pin connectors), reducing the chances of leaks, eliminating custom cables, and simplifying assembly. The new camera head also provides additional voltages for the HIT1-CCD hybrid image sensor. Daniel Lang designed the PC boards and Garrett Katzenstein designed the enclosure for the new camera head. The new camera head has been assembled and tested and is working with the KFS CCD image sensor.

4.4 HIT1-CCD image sensor

In the summer of 2003, ImagerLabs delivered the 1st prototypes of Hybrid Imaging Technology (HIT1-CCD) sensors to Caltech. This novel sensor exploits the high fill factor and Quantum Efficiency (QE) of light detection provided by silicon CCD technology coupled with the low-noise analog amplification and signal preprocessing provided by CMOS. The noise vs. framing rate design specifications for the HIT1-CCD device compared to the earlier KFS CCD are shown in the table below.

Parameter	KFS CCD	HIT1-CCD	Units
CCD output taps	32	256	-
Output Ports	32	32	-
Noise @ 50 fps	16	< 5	Electrons rms
Noise @ 100 fps	20	< 6	Electrons rms
Noise @ 200 fps	26	< 10	Electrons rms

The 8-fold increase in the number of output channels (total of 256) at the CCD-to-CMOS interface decreases the readout bandwidth by a factor of 8, giving approximately a factor of 2.83 reduction in the readout noise, for a given framing rate. An image of the HIT1-CCD image sensor is shown in Fig. 28.

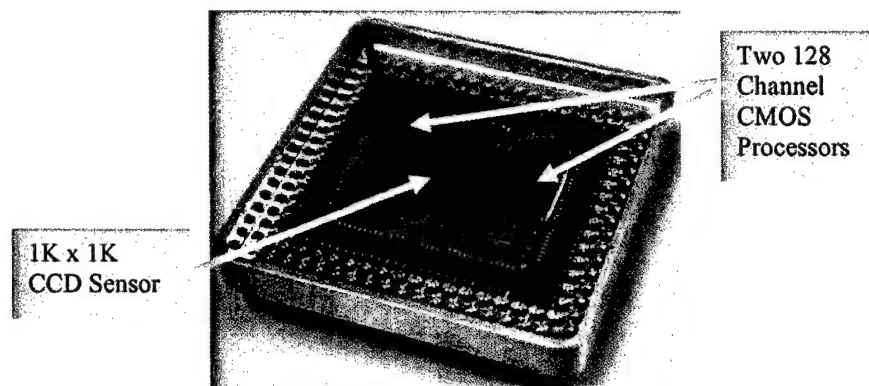


Figure 28: HIT1 hybrid CCD/CMOS image sensor

Mark Wadsworth designed the CCD image sensor and Gene Atlas of ImagerLabs designed the CMOS processors. Two CMOS processors are bump-bonded to the top and bottom of the HIT1-CCD chip using Indium balls. Each CMOS processor provides amplification, filtering and Correlated Double Sampling (CDS) for 128 input channels. The 128 processed signals are multiplexed down to 16 output channels. The 32 processed channels (16 at the top and 16 at the bottom) are fed out of the HIT1-CCD image sensor package and then processed by the present 32 channel A/D converter system. The CMOS processors have selectable input filters optimized for 30 and 200 fps. A schematic of the architecture of the device is shown in Fig. 29.

4.5 Project status

The camera head for the HIT1-CCD was completed at Caltech with all electronics tested. They appear to be working correctly. After testing the initial HIT1-CCD prototypes at Caltech, it became evident that the devices had a problem.

ImagerLabs separated the HIT1-CCD devices and discovered that the CMOS-CCD interconnects were shorted to the neighboring interconnects. The problem was tracked to the hybrid service vendor. It was determined that an incorrect tool was used for the interconnect, which resulted in the shorting (the interconnects were larger than specified).

The following describes work completed since the end of this grant, or work presently in progress, and is included below to bring the present status report up to date.

To gain control of the critical hybridization step, ImagerLabs subsequently developed the process technique in-house for self-sufficiency and enhanced quality control. February 2004, ImagerLabs acquired the necessary equipment and tooling for interconnect deposition, alignment, and

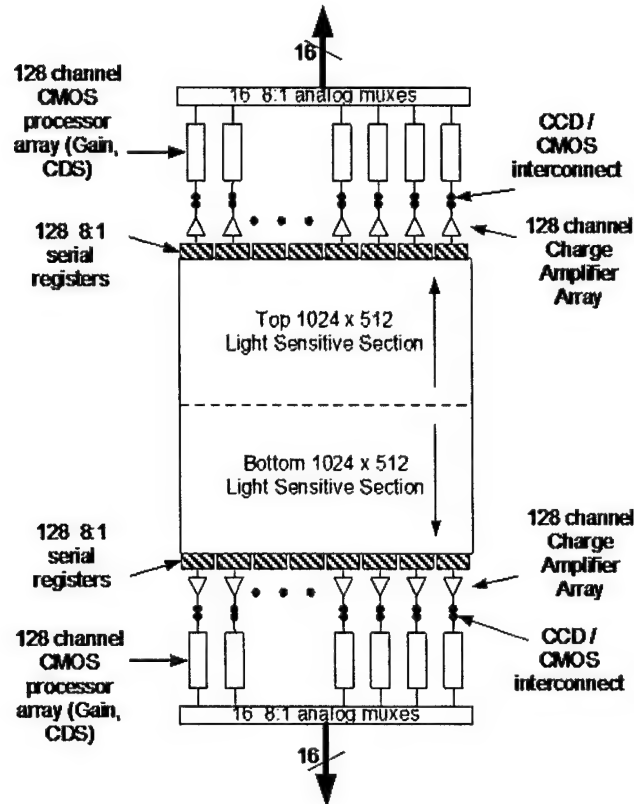


Figure 29: HIT-1 hybrid CCD/CMOS image sensor architecture

hybridization of the devices. Since February, ImagerLabs has installed and tuned the equipment for hybridization. The progress is shown in the following table:

Date	Milestone	Costs
Feb. 18	Fully operational bonder/hybridization tools	
Mar. 8	1st successful single-channel HIT1-CCD	7 scrap 1-channel CMOS processors
Mar. 19	3 successive perfect 1-channel HIT1-CCDs	0 defects
Mar. 26	1st successful 8-channel CMOS processor	10 scrap 8-channel CMOS processors

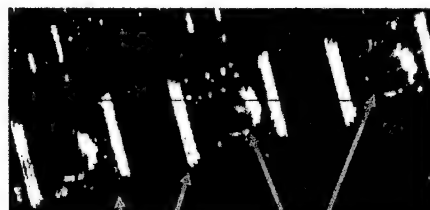
Difficulties of bond placements on long devices have been addressed and correction algorithms have been developed for optical angular misalignments. This progress was achieved using cheaper and more readily available single-channel and small multi-channel CMOS processors and CCDs from ImagerLabs' stock of devices. The expensive 1024×1024 CCDs and 128-channel CMOS processors have been reserved for the very end, pending full qualification of the process. The bonding problem is illustrated in Fig. 30.

ImagerLabs feels comfortable enough with the equipment and process expertise to begin hybridization attempts on the Caltech HIT1-CCD sensors. ImagerLabs expects to deliver the 1st internally bonded HIT1-CCD prototype to Caltech by mid-April 2004. Chances of success for an unshorted HIT1-CCD device in the 1st attempt are rated at greater than 75%. There is enough material on hand to deliver an additional 4 devices, if needed. The probability of delivering 2 unshorted HIT1-CCD devices is estimated to be greater than 95%.



IMAGERLABS

Old Bonds and Samples from new tool, 175um pad pitch



Top View – No
Shorts

Pads

Balls



Top View Shorts

Figure 30: Indium bump-bonds

4.6 High-speed disk array

The High-speed disk array development has been co-funded by the NSF TeraVoxel MRI grant (grant # EIA-0079871)

The current KFS data acquisition system has 4 GB of high-speed memory, as discussed above. For most applications, this is sufficient for imaging in two dimensions, as a function of time, at low to moderate frame rates. For imaging 3-dimensional voxels, or for long-duration recording, the data requirements increase by a factor of 20 to 100, exceeding the memory capacity of the current data-acquisition system. Jan Lindheim of CACR has developed a Datawulf storage array as part of our NSF-funded TeraVoxel project. Each Datawulf storage array is based on a high-end PC with 64-bit PCI slots, 2 Raid disk controllers, 14 low cost Ultra-ATA disk drives of 250 GB each, and a Gigabit Ethernet interface, for a storage capacity of 3 TB per array, for a total of 24 TB.

At this writing, an S-Link interface between the A/D converter boards and the Datawulf storage arrays is under development. The S-Link (Simple Link) was developed by CERN and provides a low-overhead high-speed (128 MB/s) fiber-optic data pipe from a source node to a destination node. Eight S-Links provides a maximum aggregate transfer rate of 1 gigabyte per second which is sufficient to allow 800 to 1000 frames/second when data compression is enabled. The eight Datawulf storage arrays provide a total of 24 terabytes of storage, allowing us to increase the maximum run time by a factor of 6000.

The following S-Link boards have been purchased (10 each):

- CT-ODIN-3LSC1 S-Link Source Card (128MB/s, 1 fiber pair)
- CT-ODIN-3LDC1 S-Link Destination Card (128MB/s, 1 fiber pair), and,
- S32PCI64 S-Link to 64-bit PCI adapter card.

Each S-Link destination card plugs into a S32PCI64 adapter card, which then plugs a PCI slot on one of the Datawulf storage nodes. Each S-Link source card is mounted to a VXIADC2 A/D converter board using an ADC2SLINK adapter board designed by Daniel Lang. The software to read the data from the S-Link destination card and store it into the disk array is under development at the time of this writing.

5 Conclusions

The research and work summarized in this report, along with publications that have archived the results and conclusions, have focused on turbulent mixing, with and without chemical reactions and combustion, in both liquids and gases, in flows ranging from incompressible to compressible (supersonic). The results derive from a variety of experiments and numerical simulations. Invited and contributed articles that review the overarching issues arising in the work supported by this grant were recently published (Dimotakis 2000, 2001, 2002; Hill et al. 2003), or have been submitted and are presently under review (Dimotakis 2004). These papers discuss and highlight the importance of mixing in a variety of turbulent-flow phenomena of special interest to air-breathing propulsion, in general, and high-speed and hypersonic air-breathing propulsion, in particular.

Follow-on work in progress at this writing is part of a continuing effort under AFOSR sponsorship (Grant FA9550-04-1-0020) and focuses the research further to high-speed and hypersonic propulsion. It also leverages other work at Caltech, such as at the DOE ASCI Center, and elsewhere, that also concentrates on related issues and goals.

6 Acknowledgements and other funding

We would like to acknowledge discussions and other assistance and contributions by Profs. David Goodwin, Dan Meiron, and Dale Pullin, at Caltech, as identified in the main body of this report. Major portions of the work and research performed as part of this grant were cofunded from various sources.

- The numerical simulations on hydrocarbon stagnation flow and flames (Sec. 1.2), on supersonic-flow mixing (Sec. 2.1), and on Rayleigh-Taylor Instability flows (Sec. 3) were cofunded through the Caltech DOE/ASCI Alliance Center,
 - DOE Contract W-7405-ENG-48.
- The digital-imaging and data-acquisition parts of the effort (Sec. 4) were cofunded by
 - DURIP Grant F49620-95-1-0199,
 - AFOSR Grant F49620-03-1-0102, and
 - NSF TeraVoxel MRI Grant EIA0079871000.

This part of the work was carried out with assistance by Mark Wadsworth of JPL, Brian Kern and Steve Kaye, and Caltech's Center for Advanced Computing Research (CACR), as identified in the main body of the report. Other assistance and collaborations are identified in the personnel listing, below (Sec. 7).

Further cofunding was provided to this effort, throughout the period of performance, by Caltech John K. Northrop Chair funds, whose support is also gratefully acknowledged.

References

- G. K. BATCHELOR, 1967. *An Introduction to Fluid Dynamics*. Cambridge University Press.
- J. M. BERGTHORSON AND P. E. DIMOTAKIS, 2003. An experimental and numerical study of impinging jets and reacting stagnation flow. *Western States Section of the Combustion Institute, Fall Meeting*. Paper 03F-5.
- J. M. BERGTHORSON, D. G. GOODWIN, AND P. E. DIMOTAKIS, 2004. Particle streak velocimetry and CH laser-induced fluorescence diagnostics in strained, premixed, methane-air flames. 30th *International Symposium on Combustion*, (submitted).
- K. J. BOSSCHAART AND L. P. H. DE GOEY, 2004. The laminar burning velocity of flames propagating in mixtures of hydrocarbons and air measured with the heat flux method. *Combust. Flame*, 136:261-269.
- A. W. COOK AND P. E. DIMOTAKIS, 2001. Transition stages of Rayleigh-Taylor instability between miscible fluids. *J. Fluid Mech.*, 443:69-99.
- R. M. DAVIES AND G. I. TAYLOR, 1950. The mechanics of large bubbles rising through extended liquids and through liquids in tubes. *Proc. R. Soc. Lond. A*, 200:375-390.
- M. S. DAY AND J. B. BELL, 2000. Numerical simulation of laminar reacting flows with complex chemistry. *Combust. Theory Modelling*, 4:535-556.
- P. E. DIMOTAKIS, F. D. DEBUSSY, AND M. M. KOOCHESFAHANI, 1981. Particle streak velocity field measurements in a two-dimensional mixing layer. *Phys. Fluids*, 24:995-999.
- P. E. DIMOTAKIS, 1991. Turbulent free shear layer mixing and dynamics. In *High-Speed Flight Propulsion Systems*, Progress in Astronautics and Aeronautics, chapter 5. AIAA.
- P. E. DIMOTAKIS, 2000. The mixing transition in turbulent flows. *J. Fluid Mech.*, 409:69-98.
- P. E. DIMOTAKIS, 2001. Recent advances in turbulent mixing. In *Mechanics for a New Millennium* (ICTAM Symposium Proceedings, Kluwer AP, Netherlands), pp. 327-344.
- P. E. DIMOTAKIS, 2002. Challenges in turbulent mixing and combustion. In *Turbulent Mixing and Combustion* (IUTAM Symposium Proceedings, Kluwer AP, Netherlands), pp. 95-112.
- P. E. DIMOTAKIS, 2004. Turbulent mixing. *Ann. Rev. Fluid Mech.* (submitted).
- F. N. EGOLFOPOULOS, 1994. Geometric and radiation effects on steady and unsteady strained laminar flames. *Proc. Comb. Inst.*, 25:1375-1381.
- S. K. GODUNOV, 1959. A finite difference method for the computation of discontinuous solutions of the equations of fluid dynamics. *Mat. Sb.*, 47:357-393.
- D. G. GOODWIN, 2003. An open-source, extensible software suite for CVD process simulation. In *Proc. of CVD XVI and EuroCVD Fourteen, Electrochem. Soc.*
- J. C. HERMANSON AND P. E. DIMOTAKIS, 1989. Effects of heat release in a turbulent, reacting shear layer. *J. Fluid Mech.*, 199:333-375.

- J. C. HERMANSON, M. G. MUNGAL, AND P. E. DIMOTAKIS, 1987. Heat release effects on shear-layer growth and entrainment. *AIAA Journal*, 25(4):578-583.
- D. HILL, T. W. MATTNER, C. PANTANO, A. W. COOK, P. E. DIMOTAKIS, D. I. MEIRON, AND D. I. PULLIN, 2003. Computational study of turbulent mixing at the Caltech ASC center. *AIAA Paper* 2003-3696.
- R. J. KEE, J. A. MILLER, G. H. EVANS, AND G. DIXON-LEWIS, 1988. A computational model of the structure and extinction of strained, opposed flow, premixed methane-air flames. *Proc. Comb. Inst.*, 22:1479-1494.
- A. A. KONNOV, M. IDIR, J. L. DELFAU, AND C. VOVELLE, 1996. Experimental study of extinction of nonadiabatic counterflow premixed flames. *Combust. Flame*, 105:308-320.
- L. W. KOSTIUK, K. N. C. BRAY, AND R. K. CHENG, 1993. Experimental study of premixed turbulent combustion in opposed streams: Part I - non-reacting flow field. *Combust. Flame*, 92:377-395.
- C. K. LAW, S. ISHIZUKA, AND M. MIZOMOTO, 1981. Lean-limit extinction of propane/air mixtures in the stagnation-point flow. *Proc. Comb. Inst.*, 18:1791-1798.
- C. K. LAW, C. J. SUNG, G. YU, AND R. L. AXELBAUM, 1994. On the structural sensitivity of purely strained planar premixed flames to strain rate variations. *Combust. Flame*, 98:139-154.
- P. A. LIBBY, 1998. Premixed laminar flames in impinging flows. *Combust. Sci. Technol.*, 131:345-379.
- T. W. MATTNER AND P. E. DIMOTAKIS, 2003. Large eddy simulations of miscible Rayleigh-Taylor instability. *Large Eddy Simulation, Subgrid-Scale (LES-SGS) modeling Workshop* (Caltech, 8-9 December 2003).
- T. W. MATTNER, D. I. PULLIN, AND P. E. DIMOTAKIS, 2004. Large eddy simulations of miscible Rayleigh-Taylor instability. *9th International Workshop on the Physics of Compressible Turbulent Mixing* (19-23 July 2004, Cambridge, UK), (submitted).
- A. MISRA AND D. I. PULLIN, 1997. A vortex-based subgrid stress model for large-eddy simulation. *Phys. Fluids*, 9:2443-2454.
- M. G. MUNGAL AND P. E. DIMOTAKIS, 1984. Mixing and combustion with low heat release in a turbulent shear layer. *J. Fluid Mech.*, 148:349-382.
- D. I. PULLIN, 2000. A vortex-based model for the subgrid flux of a passive scalar. *Phys. Fluids*, 12:2311-2319.
- G. P. SMITH, D. M. GOLDEN, M. FRENKLACH, N. W. MORIARTY, B. EITENEER, M. GOLDBERG, C. T. BOWMAN, R. K. HANSON, S. SONG, JR. W. C. GARDINER, V. V. LISSIAANSKI, AND Z. QIN, 2003. Gri-mech 3.0. http://www.me.berkeley.edu/gri_mech/.
- C. J. SUNG, J. S. KISTLER, M. NISHIOKA, AND C. K. LAW, 1996a. Further studies on effects of thermophoresis on seeding particles in ldv measurements of strained flames. *Combust. Flame*, 105:189-201.

- C. J. SUNG, C. K. LAW, AND R. L. AXELBAUM, 1994. Thermophoretic effects on seeding particles in ldv measurements of flames. *Combust. Sci. Technol.*, 99:119–132.
- C. J. SUNG, J. B. LIU, AND C. K. LAW, 1996b. On the scalar structure of nonequidiffusive premixed flames in counterflow. *Combust. Flame*, 106:168–183.
- J. H. TIEN AND M. MATALON, 1991. On the burning velocity of stretched flames. *Combust. Flame*, 84:238–248.
- A. G. TOMBOULIDES, J. C. Y. LEE, AND S. A. ORSZAG, 1997. Numerical simulation of low mach number reactive flows. *J. of Sci. Comp.*, 12:139–167.
- C. M. VAGELOPOULOS, F. N. EGOLFOPOULOS, AND C. K. LAW, 1994. Further considerations on the determination of laminar flame speeds with the counterflow twin-flame technique. *Proc. Comb. Inst.*, 25:1341–1347.
- B. VAN LEER, 1984. On the relation between the upwind-differencing schemes of godunov, engquist-osher and roe. *SIAM J. Sci. Stat. Comput.*, 5(1):1–20.
- T. VOEKL, D. I. PULLIN, AND D. C. CHAN, 2000. A physical-space version of the stretched-vortex subgrid-stress model for large-eddy simulation. *Phys. Fluids*, 12:1810–1825.
- C. K. WESTBROOK AND F. L. DRYER, 1981. Simplified reaction mechanisms for the oxidation of hydrocarbon fuels in flames. *Combust. Sci. Technol.*, 27:31–43.
- C. K. WU AND C. K. LAW, 1984. On the determination of laminar flame speeds from stretched flames. *Proc. Comb. Inst.*, 20:1941–1949.
- I. YAMAOKA AND H. TSUJI, 1984. Determination of burning velocity using counterflow flames. *Proc. Comb. Inst.*, 20:1883–1892.
- I. YAMAOKA AND H. TSUJI, 1988. Extinction of near-stoichiometric flames diluted with nitrogen in a stagnation flow. *Proc. Comb. Inst.*, 22:1565–1572.
- D. L. ZHU, F. N. EGOLFOPOULOS, AND C. K. LAW, 1988. Experimental and numerical determination of laminar flame speeds of methane/(Ar, N₂, CO₂)-air mixtures as function of stoichiometry, pressure, and flame temperature. *Proc. Comb. Inst.*, 22:1537–1545.

7 Personnel

7.1 Research personnel supported under this grant

- Bergthorson, Jeffrey M., Graduate Research Assistant, Aeronautics.
- Dahl, Earl E., Consultant (retired Member of the Technical Staff), Aeronautics.
- Dimotakis, Paul E., John K. Northrop Professor of Aeronautics & Professor of Applied Physics (PI).
- Gurret, Benoit-Emmanuel, Special Graduate Student (1 March – 31 July 2002), Aeronautics.
- Iglesias, Erik, Graduate Research Assistant, Aeronautics.
- Johnson, Michael B., Graduate Research Assistant, Aeronautics.
- Katzenstein, Garrett P., Research Engineer, Aeronautics.
- Lang, Daniel B., Research Engineer, Aeronautics.
- Matheou, George, Graduate Research Assistant, Aeronautics. Co-funded by the Caltech DOE/ASCI Center.
- Mattner, Trent W., Post-Doctoral Research Fellow, Aeronautics (through 15 November 2003). Presently, Post-doctoral Research Fellow, Mathematics, U. Adelaide.
- Patel, Amish, Undergraduate Research Assistant, Aeronautics.
- Shan, Jerry W., Graduate Research Assistant, Aeronautics (through 1 May 2001). Post-Doctoral Scholar, Aeronautics (May through August 2001). Presently, Assistant Professor, Rutgers University.
- Sone, Kazuo, Graduate Research Assistant, Aeronautics. Co-funded by the Caltech DOE/ASCI Center.
- Su, Wei-Jen, Graduate Research Assistant, Aeronautics (through 10 June 2001).
- Thoupupuarachchi, Chirath, Undergraduate Research Assistant, Aeronautics.
- Vagelopoulos, Christina, Post-Doctoral Research Fellow, Aeronautics (through 4 May 2001). Presently with the Combustion Research Facility (CRF), Sandia (Livermore, CA).

7.2 Other collaborators

- Atlas, Gene, President and CEO, ImagerLabs. HIT1-CCD CMOS section design and HIT1-CCD device integration.
- Collins, S. Andrew, Jet Propulsion Laboratory. Collaborator on digital imaging, and KFS development and project management.
- Cook, Andrew W., Lawrence Livermore National Laboratory. Collaborator on direct numerical simulations of three-dimensional, variable-density flows.

- Deiterding, Ralph, Member of the Technical Staff, Center for Advanced Computing Research, Caltech. Collaborator on compressible-flow/-turbulence simulations (Sec. 2.2).
- Elliott, S. Thomas, Jet Propulsion Laboratory. Collaborator on digital imaging and KFS-CCD development and testing.
- Goodwin, David G., Prof. Mechanical Engineering and Applied Physics, Caltech. Collaborator on direct-numerical simulations of hydrocarbon flames and developer of Cantera software platform (Sec. 1.1).
- Kern, Brian, Graduate Research Assistant, Astronomy, Caltech. Collaborator in the high framing-rate imaging (KFS) development (Sec. 4).
- Lombeyda, Santiago, Member of the Technical Staff, Center for Advanced Computing Research (CACR), Caltech. Collaborator on 3-D computer visualization.
- Martin, Christopher, Prof. Physics, Caltech. Collaborator in the high-framing-rate imaging (KFS) development.
- Meiron, Daniel I., Prof. Computational & Applied Mathematics, and Computer Science, Caltech. Collaborator and co-advisor on stagnation-flame (Sec. 1.2) and compressible-turbulence (Sec. 2.2) simulations.
- Miller, Paul L., Lawrence Livermore National Laboratory. Collaborator on the work on Rayleigh-Taylor instability flows (Sec. 3), as well as turbulent mixing in a variety of compressible and incompressible-turbulence contexts.
- Pantano, Carlos, Post-Doctoral Scholar, Aeronautics. Collaborator on compressible-flow/-turbulence simulations (Sec. 2.2).
- Papalexandris, Milto V., Assistant Professor, U. Catholique de Louvain. Collaborator on compressible-flow/-turbulence simulations (Sec. 2.2).
- Patton, James M., Member of the Technical Staff, Center for Advanced Computing Research (CACR), Caltech. Collaborator on high-capacity data storage and 3-D computer visualization (Sec. 4.6).
- Pullin, Dale I., Professor, Aeronautics. Collaborator on LES-SGS simulations of Rayleigh-Taylor instability flows (Sec. 3).
- Shan, Jerry W., Assistant Professor, Rutgers University.
- Wadsworth, Mark, originally, JPL (digital imaging), and, presently, President of Tangent Technologies. Principal designer of kilo-frame/sec (KFS) CCD focal-plane array.

8 Publications and reports of work supported under this grant

J. M. BERGTHORSON AND P. E. DIMOTAKIS, 2003a. An experimental and numerical study of impinging jets and reacting stagnation flow. *Western States Section of the Combustion Institute, Fall Meeting*. Paper 03F-5.

- J. M. BERGTHORSON AND P. E. DIMOTAKIS, 2003b. An experimental and numerical study of impinging jets in cold and reacting stagnation flow. *Bull. Am. Phys. Soc.*, 48(10):106. Abstract EL.009.
- J. M. BERGTHORSON, D. G. GOODWIN, AND P. E. DIMOTAKIS, 2004. Particle streak velocimetry and CH laser-induced fluorescence diagnostics in strained, premixed, methane-air flames. 30th *International Symposium on Combustion*, (submitted).
- A. W. COOK AND P. E. DIMOTAKIS, 2001. Transition stages of Rayleigh-Taylor instability between miscible fluids. *J. Fluid Mech.*, 443:69–99.
- P. E. DIMOTAKIS, 2000. The mixing transition in turbulent flows. *J. Fluid Mech.*, 409:69–98.
- P. E. DIMOTAKIS, 2001. Recent advances in turbulent mixing. In *Mechanics for a New Millennium* (ICTAM Symposium Proceedings, Kluwer AP, Netherlands), pp. 327–344.
- P. E. DIMOTAKIS, 2002. Challenges in turbulent mixing and combustion. In *Turbulent Mixing and Combustion* (IUTAM Symposium Proceedings, Kluwer AP, Netherlands), pp. 95–112.
- P. E. DIMOTAKIS, H. J. CATRAKIS, AND D. C. FOURGUETTE, 2001. Flow structure and optical beam propagation in high reynolds number, gas-phase shear layers and jets. *J. Fluid Mech.*, 433: 105–134.
- F. N. EGOLFOPOULOS AND P. E. DIMOTAKIS, 2001. A comparative study of ethylene kinetics in premixed and non-premixed flames. *Combust. Sci. Technol.*, 162:19–36.
- D. HILL, T. W. MATTNER, C. PANTANO, A. W. COOK, P. E. DIMOTAKIS, D. I. MEIRON, AND D. I. PULLIN, 2003. Computational study of turbulent mixing at the Caltech ASC center. *AIAA Paper* 2003–3696.
- M. B. JOHNSON AND P. E. DIMOTAKIS, 2001. Aerodynamic control of a subsonic diffuser. *Bull. Am. Phys. Soc.*, 46(10):179. Abstract JL.12.
- B. KERN, P. E. DIMOTAKIS, D. B. LANG, C. MARTIN, AND R.N. THESSIN, 2003. Aberrating medium characterization and image reconstruction with a quadrature-phase interferometer. *AIAA Paper* 2003–3610.
- B. KERN, D. B. LANG, C. MARTIN, P. E. DIMOTAKIS, AND M. WADSWORTH, 2001. A high-speed quadrature-phase rotation-shearing interferometer for imaging through turbulence. *AIAA Paper* 2001–2797.
- T. W. MATTNER AND P. E. DIMOTAKIS, 2003a. Large eddy simulations of miscible Rayleigh-Taylor instability. *Large Eddy Simulation, Subgrid-Scale (LES-SGS) modeling Workshop* (Caltech, 8–9 December 2003).
- T. W. MATTNER AND P. E. DIMOTAKIS, 2003b. Variable density ratio simulations of miscible Rayleigh-Taylor instability. *Bull. Am. Phys. Soc.*, 48(10):79–80. Abstract DP.005.
- M. V. PAPALEXANDRIS, A. LEONARD, AND P. E. DIMOTAKIS, 2002. Unsplit algorithms for multi-dimensional systems of hyperbolic conservation laws with source terms. *Comp. & Math. w. Applications*, 44:25–49.

- J. W. SHAN, 2001. *Mixing and Isosurface Geometry in Turbulent Transverse Jets*. California Institute of Technology, Ph.D. thesis.
- J. W. SHAN AND P. E. DIMOTAKIS, 2001. Turbulent mixing in liquid-phase transverse jets. *GALCIT Fluid Mechanics Report*, <http://resolver.library.caltech.edu/CaltechGalcitFM:2001.006>.
- W.-J. SU, 2001. *Aerodynamic Control for a Subsonic Diffuser*. California Institute of Technology, Eng. thesis.

9 Collaborations, interactions, and transitions

Consultative and advisory functions to other labs and government agencies:

- Dimotakis, P. E., Lawrence Livermore National Laboratories. Consulting on compressible turbulence and inertial-confinement fusion (1993-present).
- Dimotakis, P. E., JASON group, MITRE (1997 to present). Consulting to DARPA and other US Government agencies.
- Dimotakis, P. E., General Atomics, San Diego, CA. High-energy lasers and thermal management.

Interactions with:

- Buckley, Parker L., Chief, Aerospace Propulsion Office, Wright-Patterson AFB. Discussions/exchanges on hypersonic propulsion.
- Carter, Cambell, Wright-Patterson AFB. Discussions on scramjet injection/mixing.
- Edwards, James T., Wright-Patterson AFB. Discussions/exchanges on hypersonic-propulsion fuels issues.
- Jackson, Thomas, AFRL/PRA, Wright-Patterson AFB. Discussions on scramjet injection, mixing, and possibilities for joint experiments at AFRL.
- Katta, Viswanath R. (Vish), AFRL/WP - Innovative Scientific Solutions, Inc. Discussions/exchanges on hydrocarbon-flame simulations.
- Mercier, Robert A., Deputy for Technology, AFRL/PRA, Wright-Patterson AFB. Discussions/exchanges on hypersonic propulsion.
- Roquemore, (William) Melvyn, AFRL, Wright-Patterson AFB. Discussion/exchanges on hydrocarbon-flame simulations and high-energy laser propulsion applications.

Transitions (cases where knowledge resulting from this research has, is, or will be used in a technology application): No commercial transitions.

- Contributions to High-Energy Laser (HEL) development (1970-90). Contact: Dr. Wilhelm Behrens (310 812-0468), TRW R1-1044, 1 Space Park, Redondo Beach, CA 90278.
 - i. Shear-layer growth and entrainment data/models.

- ii. Reynolds-number effects on mixing.
- iii. Use of gas-mixtures for index-of-refraction matching.
- iv. Laser-induced fluorescence diagnostics.

New discoveries, inventions, patents: None

10 Honors/awards

- Dimotakis, P. E.:
 - John K. Northrop Chair, Aeronautics, Caltech (February 1995).
 - Associate Fellow, AIAA (June 1989).
 - Fellow, American Physical Society (November 1980).
- Kern, B.
 - Michelson Fellowship, Jet Propulsion Laboratory, California Institute of Technology.
- Shan, J. L.:
 - Ph.D., California Institute of Technology (June 2001).
- Su, W.-J.:
 - Engineers' degree, California Institute of Technology (June 2001).